SECURITY INFORMATION

CONFIDENTIAL

Copy 3
RM SL53F15

NACA

RESEARCH MEMORANDUM

for the

Bureau of Aeronautics, Department of the Navy

THE EFFECTS OF EXTENSIBLE ROCKET RACKS ON LIFT, DRAG, AND STABILITY OF A 1/10-SCALE ROCKET-BOOSTED MODEL OF THE MCDONNELL XF3H-1 AIRPLANE FOR A MACH NUMBER RANGE OF 0.60 TO 1.34

TED NO. NACA DE 31

By Norman L. Crabill

Langley Aeronautical Laboratory
Langley Field, Va.

NATIONAL ADVISORY COMMITTEE
FOR AERONAUTICS
WASHINGTON

JAN 1953

CONFIDENTIAL

NATIONAL ADVISORY COMMITTEE FOR AERONAUTICS

RESEARCH MEMORANDUM

for the

Bureau of Aeronautics, Department of the Navy

THE EFFECTS OF EXTENSIBLE ROCKET RACKS ON LIFT, DRAG, AND STABILITY OF A 1/10-SCALE ROCKET-BOOSTED MODEL OF THE MCDONNELL XF3H-1 AIRPLANE FOR A MACH NUMBER RANGE OF 0.60 TO 1.34

TED NO. NACA DE 31

By Norman L. Crabill

SUMMARY

The results of the first test by the National Advisory Committee for Aeronautics on the transonic longitudinal characteristics of a 1/10-scale rocket model of the McDonnell XF3H-1 airplane are presented in this report. The model, flown with a center-of-gravity location of 28.5 percent of the mean aerodynamic chord and a stabilizer setting of -5.91° relative to the wing chord plane, was equipped with extensible rocket racks. In the test, which utilized the freely flying rocket-boosted model technique, the Mach number varied from 0.60 to 1.34, and the Reynolds number varied from 4.5 to 11 $\times 10^6$.

The effects of the rocket racks in the extended position on the trim and static lift, drag, and stability were generally small and within the accuracy of the data. However, at low supersonic speeds, the racks caused an increment of about 0.012 in total-drag coefficient and were evidently responsible for some turbulence which gave rise to some light buffet and apparently variable dynamic stability. Below a Mach number of 0.88 and above a lift coefficient of 0.60, the model became statically unstable and pitched up past the stall. The usual longitudinal parameters and derivatives describing lift, drag, and stability of the model, as measured in this test, are given as functions of Mach number. In addition, the pressure recovery of the inlet at zero mass flow and an approximation to the static directional stability derivative are given. In general, the results of this test agree with the results of tests on similar models in wind tunnels.

INTRODUCTION

As part of the general external-stores program at Langley Aeronautical Laboratory, the NACA is testing 1/10-scale models of the McDonnell XF3H-1 airplane equipped with internally stowed extensible rocket racks. These tests are being performed to determine what effect the presence of these rocket racks will have on the lift, drag, trim, and stability of the model while flying at transonic speeds. The results of the first test are presented herein.

The model was supplied by the McDonnell Aircraft Corporation, and the test was conducted by personnel of the Pilotless Aircraft Research Division of the Langley Aeronautical Laboratory and at its testing station at Wallops Island, Va.

SYMBOLS

a_l acceleration parallel to wing chord plane at center of gravity, positive toward tail, ft/sec^2

a_n acceleration perpendicular to wing chord plane at center of gravity, positive upward, ft/sec^2

a_t acceleration perpendicular to plane of symmetry, near center of gravity, positive toward right wing tip, ft/sec^2

b wing span, ft

C_C chord force coefficient, $\frac{a_l}{g}\frac{W}{qS_{wing}}$

C_D total-drag coefficient, $C_N \sin\alpha + C_C \cos\alpha$

C_L total-lift coefficient, $C_N \cos\alpha - C_C \sin\alpha$

C_m pitching-moment coefficient, positive for a moment tending to raise nose $\frac{\text{Pitching moment}}{qS_{wing}\bar{c}}$

C_n yawing-moment coefficient, $\frac{\text{Yawing moment}}{qS_{wing}b}$

C_N normal-force coefficient, $\frac{a_n}{g}\frac{W}{qS_{wing}}$

C_Y lateral-force coefficient, $\frac{a_t}{g}\frac{W}{qS_{wing}}$

$\bar{c}$ wing mean aerodynamic chord, ft

g acceleration due to gravity, 32.2 ft/sec^2

I_X mass moment of inertia of model about longitudinal principal axis, slug-ft^2

I_Y mass moment of inertia of model about transverse axis, slug-ft^2

I_Z mass moment of inertia of model about axis perpendicular to longitudinal principal axis and transverse axis, slug-ft^2

l vertical distance from center of gravity of model to centroid of exposed frontal area of rocket rack of any rack extension, ft

M free-stream Mach number

P period of motion, sec

q dynamic pressure, 0.7(atmospheric static pressure)M^2, lb/ft^2

$q = \frac{1}{57.3}\frac{d\theta}{dt}\frac{\bar{c}}{2V}$

R Reynolds number based on wing mean aerodynamic chord

S area, sq ft

T time, sec

$T_{1/2}$ time for amplitude of motion to damp to one-half initial value, sec

V free-stream velocity, ft/sec

W weight of model, lb

α angle of attack of wing chord plane, positive nose up, deg

$$\dot{\alpha} = \frac{1}{57.3} \frac{d\alpha}{dt} \frac{\bar{c}}{2V}$$

β angle of sideslip, positive for relative wind coming from right, deg

δ_{RR} angular extension of rocket racks, deg (see fig. 3)

δ_s angular deflection of horizontal stabilizer relative to wing chord plane, positive for trailing edge down, deg

θ angle of wing chord plane relative to horizontal, positive nose up, deg

Derivatives with respect to a quantity are indicated as shown in the following example:

$$C_{m_{C_L}} = \frac{dC_m}{dC_L}$$

Increments are denoted by Δ, for example:

$\Delta C_{L_{trim}}$ = Increment in trim lift coefficient

In addition, a few descriptive subscripts are used:

base fuselage base

RR rocket racks (see fig. 3)

trim trim condition

wing total wing

DESCRIPTION OF MODEL AND APPARATUS

Model

A 1/10-scale model of the McDonnell XF3H-1 airplane was used in this test. The outline drawing of figure 1 and the photographs of figure 2 indicate the principal features of the model. Unlike the full-scale airplane, the model had no wing fences, slots, or moveable controls, and the ducts were blocked completely just inside the inlet and at the

jet exit. The center of gravity was at 28.5 percent of the mean aerodynamic chord and 0.012 chord length above the model center line. The horizontal stabilizer was fixed at -5.91° relative to the wing chord plane. Table I lists the pertinent physical properties and dimensions of the model. Briefly, the model construction was as follows: wing - laminated mahogany and aluminum-alloy spar and trailing-edge insert, fuselage - semimonocoque with aluminum-alloy skin and steel and aluminum-alloy bulkheads, horizontal and vertical stabilizers - solid-aluminum alloy, and canopy and fairings - laminated and solid mahogany finished with clear lacquer.

Rocket Racks

The rocket-rack configuration tested is shown in figure 3. The frontal area of both racks, when extended by rotating through an angle of 114.3° was 0.022 square foot. Other pertinent dimensions are given in figure 3. A hydraulically operated pulse system extended and retracted the racks in an approximate square wave motion. The time to extend the racks was generally 0.046 second, whereas the time to retract was longer, about 0.080 second. Photographs of the underside of the model with racks fully retracted and extended are shown in figure 4.

Instrumentation

The model carried a ten-channel telemeter which transmitted continuous records of the acceleration normal to the wing chord plane at the center of gravity and at the tail, the acceleration parallel to the wing chord plane near the center of gravity, the transverse acceleration, angle of attack relative to the fuselage center line, rocket-rack position, total pressure measured on the left wing tip and in the right inlet, and base pressure measured behind the angle-of-attack vane (calibrated to give atmospheric static pressure) and in the fuselage jet exit. The arrangement of the accelerometers is shown in figure 5 and the points at which the pressures were measured are shown in figure 1.

Photography, an SCR 584 radar set, and the CW Doppler velocimeter were used to observe the first part of the flight. After the flight had taken place, a radiosonde was released to determine atmospheric static temperature and pressure.

PROCEDURE

Before flying, the model was mechanically vibrated to determine the resonant frequencies and node lines (see fig. 5) of its major components.

The model was tested by the freely flying rocket-boosted model technique described in detail in reference 1. A fin-stabilized ABL Deacon rocket motor was used as the booster. Photographs of the booster-model combination before take-off and at separation are shown as figure 6.

PRECISION

In determining the probable errors in Mach number and dynamic pressure, it was assumed (on the basis of statistical data compiled by the Instrument Research Division) that the telemetered total pressure and angle-of-attack-vane base pressure were accurate to within ±2 percent of their full-scale ranges. With this assumption, the bands of scatter in the calibration curves of total-pressure–base-pressure ratio and base-pressure–atmospheric-pressure ratio determined the probable errors in Mach number and static pressure, from which the error in dynamic pressure q was determined. Then, the probable errors in C_N and C_C were computed at the trim conditions at three Mach numbers, assuming that the accelerometer errors were ±2 percent of their calibrated full-scale ranges. The maximum probable error in angle of attack is composed of the calibration error of ±2 percent of its full-scale range and an additional error due to very small structural eccentricities in the angle-of-attack vane itself. All the foregoing errors are the maximum probable errors and are shown subsequently. The actual errors are generally less. For example, experience indicates that the low-lift drag coefficient for this test should be determined within $\Delta C_D = \pm 0.001$ (see ref. 2), and that incremental quantities and slopes are affected much less than the absolute values.

MAXIMUM PROBABLE ERRORS IN ABSOLUTE VALUES

M	$\pm\Delta M$	$\pm\Delta q$	$\pm\Delta C_N$	$\pm\Delta C_C$	$\pm\Delta\alpha$
0.90	0.030	26	0.034	0.006	0.60 ± 0.50
1.10	.027	61	.023	.005	.60 ± .50
1.30	.011	22	.012	.003	.60 ± .50

From $M = 1.25$ to 1.32, the Mach number error may be slightly greater than that shown, since at $M = 1.25$ the telemetered total pressure showed a sudden loss of about 115 pounds per square foot due probably to interference from the shock wave springing from the wing root (see schlieren photographs in ref. 3, p. 12.06). The loss continued until $M = 1.27$ was reached in decelerating flight. Above $M = 1.25$, the Mach number was

determined from a calibration of the observed total-pressure–base-pressure ratio obtained during the boosted phase of the flight, with the use of a velocity derived from the CW Doppler velocimeter. At $M = 1.25$, just before the break in total pressure, the Doppler Mach number derived from the velocimeter agreed with the Mach number obtained from the total-pressure–base-pressure ratio. Hence, the error, though undetermined, is probably small.

RESULTS AND DISCUSSION

Reynolds Number

The Reynolds number of this test based on wing mean aerodynamic chord varied between 4.5×10^6 at $M = 0.60$ and 11.6×10^6 at $M = 1.34$. Figure 7 shows the Reynolds numbers at the intermediate Mach numbers.

Rocket-Rack Program

The angular position of the rocket racks δ_{RR} is given as a function of Mach number in figure 8. Because of negative normal acceleration loads in excess of the servo-piston forces, the racks were partially extended during the times when it was expected they would be completely closed. At these times the rack position was fixed and did not follow the normal acceleration because, it is believed, the drag load caused a deflection of the actuating linkage, binding the racks in a position determined by the hydraulic-accumulator pressure, the normal acceleration, and the drag load. Although the design maximum angle of extension was 114.3°, the actual maximum rack extension in flight was 122°.

Flight Time History

Booster separation occurred at $T = 3.0$ seconds after take-off. A partial time history of the subsequent flight comprising the Mach number M, the rocket-rack position δ_{RR}, the lift coefficient C_L, and the lateral-force coefficient C_Y is shown in figure 9. The curve for C_L exhibited regular damped sinusoidal oscillations only near $T = 3.3$ seconds and $T = 5.90$ seconds. The apparent neutral dynamic stability in C_Y and the apparently variable longitudinal dynamic stability in C_L near $T = 3.9$ seconds could be explained in one or more of several ways:

(1) Neutral lateral dynamic stability with lateral-longitudinal coupling near $M = 1.20$ ($T = 3.9$ seconds)

(2) Model response to turbulence created by the rocket racks and their opening in the bottom of the fuselage

(3) Model response to atmospheric turbulence

In the absence of more complete measurements, it is not possible to assess the relative magnitudes of these effects. However, it is significant that the apparent variable longitudinal dynamic stability disappeared when the racks partially closed at $T = 4.30$ seconds.

The model became statically unstable longitudinally at 6.53 seconds, and the wing stalled at 6.70 seconds. At $T = 6.74$ seconds, the angle-of-attack instrument hit its limit stop of 17°. Although the angle of attack evidently continued to increase somewhat above 17°, there is no direct evidence that the model broke up. At $M \approx 0.5$ (not shown) the model pitched down and trimmed at values of C_L approaching 0.70.

Trim

Lift coefficient.- The trim lift coefficient presented in figure 10 as a function of Mach number was determined by obtaining the mean line of the envelope of the lift coefficient plotted against time. Below $M = 0.84$, the trim normal-force coefficient is presented, since at that Mach number the angle-of-attack instrument hit its limit stop. The dashed line in figure 10 represents the trim lift coefficient obtained from the wind-tunnel data in reference 4. The various corrections applied to the wind-tunnel data to convert it to the flight conditions of this model are given in the appendix. The values of $C_{L_{trim}}$ obtained from the wind-tunnel data, are generally higher at transonic speeds and lower at supersonic speeds than the values of $C_{L_{trim}}$ obtained in the present test.

Angle of attack.- The trim angle of attack of the wing chord plane is given as a function of Mach number in figure 11. The trim angle of attack corresponding to the trim lift coefficient derived from the wind-tunnel data is plotted for comparison. Above $M = 0.90$, small changes in trim occurred coincident with the rack movement.

Effect of rocket racks on trim.- The changes in $C_{L_{trim}}$ due to changes in rocket-rack position, figure 10, are small and difficult to determine from the small-amplitude pitch oscillations. The largest change $\Delta C_{L_{trim}} = 0.007$ at $M = 1.04$ is within the accuracy of the data. Elsewhere, at $M = 0.89$, 0.96, 1.14, and 1.27, the changes in $C_{L_{trim}}$ are too small to be measured, although the wind-tunnel data,

reference 4, indicated that changes on the order of $\Delta C_{L_{trim}} = 0$, 0.020, 0.025, and 0, respectively, could be expected. The lack of agreement may be due to the method of accounting for the intermediate rack position and to the accuracy with which the increments can be determined.

The increments in α_{trim} due to the partial movement of the racks have been used to determine the incremental trim angle of attack due to the design extension of the racks by equation (2) in the appendix. This value of $\Delta\alpha_{trim}$, figure 12, decreases from -0.26° at $M = 1.04$ to -0.18° at $M = 1.14$. The point at $M = 1.27$ is questionable because of the approximate nature of the extrapolation and because of the distortion present in the angle-of-attack time history (similar to that in the time history of C_L). The point at $M = 0.96$ is also ignored because of the pitch-up occurring at that time. These changes in angle of attack are small and are within the probable absolute accuracy of the data. The solid line in figure 12 represents the trim-angle-of-attack change computed from the data in reference 4.

Lift

Lift-curve slope.- The variation of lift coefficient with angle of attack was determined at several subsonic and supersonic Mach numbers. The plots of C_L against α, figure 13, indicate that at $M = 0.95$, C_L was a linear function of α up to $C_L = 0.55$. Above this value of C_L, the slope continued to decrease as C_L increased up to the test limit, $C_L = 0.71$. At supersonic Mach numbers, the linear variation held within the test limits. The slopes of these curves are given as Mach number functions in figure 14 and are compared with slopes derived from reference 4 corresponding to $C_L = 0$ and $C_L = C_{L_{trim}}$ of this test. The effect of wing bending on the lift-curve slope has not been considered, but from a consideration of the wing thickness, construction, and wing weight it should be small.

Effect of rocket racks on lift.- The data available from this test indicate that the effect of the rack position on lift-curve slope and angle of zero lift is small. Close inspection of figure 13 will indicate that any changes in either of these quantities coincident with changes in rack position are not definitely established because of other effects, and, in any case, are within the accuracy of the data.

Buffet.- In addition to a certain amount of random interference on the order of $\pm\frac{1}{4}g$, the trace of the two normal accelerometers also

exhibited high-frequency sinusoidal oscillations varying in amplitude from $\pm\frac{1}{2}$ to $\pm 3g$. The half-amplitudes, converted to $\pm\Delta C_N$, of these oscillations are shown on figure 15 as a function of Mach number. The average frequencies of these oscillations observed at the center of gravity and the tail are 130 and 91 cycles per second, respectively. These frequencies are close to the lowest wing-body natural frequencies of approximately 120 and 85 cycles per second, respectively, observed in the ground test (see fig. 5). Because of this relationship and the fact that the onset of continuous oscillations occurred slightly before the break in the lift-curve slope at $C_L = 0.55$, (see fig. 13), it was concluded that these oscillations were largely due to wing buffet and not to the wing-bending flutter mentioned in reference 5.

Above $M = 0.91$, however, the observed buffet may have been the response of the wing to the turbulence from the rocket racks. This turbulence was evidently more pronounced at $M = 1.25$ than at $M = 1.0$ since no buffet was observed near $M = 1.0$, figure 15. It is interesting to observe that the apparently variable dynamic longitudinal stability, figure 9, occurred at the same time as the supersonic buffet, a circumstance which lends credence to the idea that the racks created turbulence at this Mach number which caused buffet and continually disturbed the model. However, no firm conclusion can be made. The amplitudes shown in figure 15 apply at the value of $C_{L_{trim}}$ of this test, figure 10. The buffet intensity for the airplane at this value of $C_{L_{trim}}$, taken from reference 6, is also shown in figure 15.

Lateral buffet, figure 16, occurred at the maximum positive and negative values of C_Y just before the wing stalled completely. The vertical-tail first bending frequency was 96 cycles per second, and the observed frequencies were 126 and 159 cycles per second. Therefore, this buffet probably was not due to flow separation over the vertical fin; it could have been due to asymmetric flow fluctuations on the wing.

Drag

Drag carpet.- The total-drag coefficient of the model, which includes base drag, is given in figure 17 for various lift coefficients and rocket-rack positions for the range of Mach numbers of this test. The influence of lift coefficient, rocket-rack position, and Mach number are readily apparent.

Base-drag coefficient.- The base-drag coefficient shown in figure 17 was calculated from the pressure observed in the closed-jet exit, assuming a flat pressure distribution over an area of 0.0767 square foot.

Variation of drag with lift.- At four Mach numbers the data were suitable for determining the variation of drag with lift. The results, figures 18 and 19, indicate that the inclination of the resultant force vector forward of the normal to the wing results in a reduction in $C_{D_{C_L}^2}$ from $1/57.3\ C_{L_\alpha}$ of 0.045 at $M = 0.95$ and 0.078 at $M = 1.29$. The solid line in figure 19 represents an estimated value of $C_{D_{C_L}^2}$ which, based on references 3, 7, and 8 and the results of this test, is used later in this report in estimating $C_{D_{min}}$.

Drag increment due to racks.- The increment in total-drag coefficient due to the presence of fully extended racks was computed according to equation (3) in the appendix except at $M = 0.89$, where an additional correction for varying lift coefficient was made. Thus, the data presented in figure 20 represent the drag penalty which would be incurred in extending the racks from a fully closed position to a fully opened position. This increment in drag coefficient is within the accuracy of the data except at $M = 1.27$, where it is about 0.012, and compares very well with the results of wind-tunnel tests of racks of slightly differing configurations (refs. 3, 7, and 8) adjusted to the frontal area of the racks of the present test by a simple area ratio.

Minimum drag coefficient.- By using the values of $C_{D_{C_L}^2}$, $C_{D_{base}}$, and $\Delta C_{D_{RR}}$ determined previously, it is possible to make an estimate of the minimum drag coefficient of the clean model. However, in order to make a comparison with the minimum drag coefficient given in reference 3, which was obtained from models having faired-over duct entrances and closed jet exits, some account must be taken of the increment in drag coefficient due to the presence of the blocked ducts. The increment in drag coefficient due to changing the mass-flow ratio from 0.9 to 0.3, given for the forebody shape of a model of this airplane in reference 9, has also been subtracted from the data of the present test. This estimate of the minimum drag coefficient together with the minimum drag coefficient from reference 3 is plotted in figure 21. Considering the differences in Reynolds number at supersonic speeds, and the many corrections which were applied to get this estimate, the agreement is very good.

Longitudinal Stability

Static stability.- The static longitudinal stability was determined by analyzing the short-period oscillations in pitch by two different methods: One method, given in reference 1, involves a knowledge of the period of the motion and gives C_{m_α}; the other method, from reference 10,

requires differentiation of the time histories of C_L and α, and gives C_m directly as a function of time, so the variation of C_m with C_L can be determined by inspection. The results of both methods were used to determine the neutral-point location.

C_{m_α}: The period and corresponding values of C_{m_α} are shown in figures 22(a) and 22(b), respectively, for the two series of regular damped sinusoidal oscillations. Also shown in figure 22(b) is the C_{m_α} at the $C_{L_{trim}}$ of the present test derived from reference 4.

$C_{M_{C_L}}$: Figure 23 shows the static pitching-moment coefficient plotted against C_L at several Mach numbers. The dotted lines in the figure represent the static pitching-moment coefficient at the C_L of this test, derived from reference 4, corrected for the effects of the actual rocket-rack position by the methods described in the appendix. It represents the predicted value of C_m for the airplane at the instantaneous values of C_L, M, and δ_{RR} of the model at mass-flow ratios approaching 1.0. Figure 23 shows that the flight model became statically unstable at $C_L = 0.60$, $M = 0.88$ and pitched up until it became stable again, above $C_L = 0.69$, $M = 0.85$. These values of C_L, 0.60 and 0.69, are slightly higher (about 0.05) than the values of C_L corresponding to the two breaks in the lift-curve slope. The $C_{N_{trim}}$ in this stalled condition was above 0.8.

Neutral point: The neutral-point locations derived from the two methods are plotted as a function of Mach number in figure 24. As the model decelerated from $M = 0.92$ to 0.87, the neutral point moved abruptly forward from 43 to 17.5 percent of the mean aerodynamic chord. This abrupt movement was probably due to the forward shift in wing aerodynamic center and to the unstable variation of downwash existing at the high angle of attack reached at this point (see ref. 4, p. 6.90). At $M = 1.3$, the neutral point was approximately at 62 percent of the mean aerodynamic chord. The agreement among the data from the two flight methods and the data from reference 4 is fair.

Dynamic stability.- In the absence of more complete measurements, it is not possible to prove that the apparently variable longitudinal dynamic stability, which occurred when the racks were fully extended near $M = 1.20$, was not due to lateral-longitudinal coupling or the response of the model to atmospheric turbulence. Since the small amplitude oscillation did not damp from $M = 1.27$ to 1.10 until the racks closed,

figure 9, and the model buffeted somewhat within this Mach number range owing, it is thought, to the effect of the racks (see fig. 15 and section entitled "Buffet"), it is possible that the racks were responsible for some turbulence or interference which created a continuous disturbance. The resulting motion, then, is simply the dynamic response of the model to a continuous disturbance. If this is true, then, the effect of the turbulence on the dynamic stability of the full-scale airplane at the same altitude (approximately 2,200 feet) would be less pronounced because of dynamic considerations. Without knowing the form of the forcing function, no analysis of the motion can be made.

From an analysis of the three oscillations which did damp (when the racks were not fully extended), the time to damp to one-half amplitude $T_{1/2}$ and the damping moment factor $C_{m_{\dot{\alpha}}} + C_{m_q}$ were computed. These quantities, and the damping moment factor estimated from the methods in reference 11, are shown as Mach number functions in figure 25. At $M = 0.95$, the estimate is within 30 percent of the observed damping; at $M = 1.31$, within about 20 percent. There is no adequate transonic theory for estimating pitch damping.

Directional Stability

An estimate of the static directional stability derivative C_{n_β} was made, with the use of the approximate equation presented in reference 12, that is

$$C_{n_\beta} = \frac{4\pi^2 I_Z}{57.3 P^2 q S_{wing} b}$$

where P is the period observed on the telemeter trace of the lateral accelerometer. This estimate together with test results from reference 3, and the estimate in reference 13, is presented in figure 26. At subsonic speeds, the estimated value of about 0.0038 from reference 13 agrees well with the value obtained in this test. At supersonic speeds, the data are severely scattered. A more detailed analysis, including lateral-longitudinal coupling effects and corrections to be applied to the indicated lateral acceleration because of the distance separating the accelerometer from the center of gravity, would be required to determine the actual supersonic C_{n_β}.

Inlet Pressure Recovery

The inlet total-pressure recovery at zero mass flow was calculated from the free-stream total pressure and the stagnation pressure observed at the pressure orifice located in the middle of the right inlet, and is given as a Mach number function in figure 27. The relatively low values, 75 percent at $M = 0.90$ to 65 percent at $M = 1.33$, were probably due to a thickened boundary layer or to boundary-layer separation immediately ahead of the inlet, since the mass flow was zero. In interpreting the abrupt change between $M = 0.90$ and $M = 0.80$, it should be kept in mind that the model angle of attack was about 6° at $M = 0.90$, and more than 15° at $M = 0.80$. Presumably, the boundary layer on the nose cone was swept away, giving high values of total-pressure recovery at the lower Mach numbers. Results of a test of the same inlet at a mass-flow ratio of 0.3, reference 9, are plotted for comparison.

It should be noted that there was a small amount of roughness on the inlet total-pressure telemeter trace, indicating possible flow fluctuations on the nose cone.

SUMMARY OF RESULTS

A freely flying 1/10-scale model of the McDonnell XF3H-1 airplane equipped with extensible rocket racks has been tested at a center-of-gravity location of 28.5 percent of the mean aerodynamic chord and a fixed stabilizer deflection of -5.91° relative to the wing chord plane. The principal results derived from this test were:

1. The effects of the rocket racks in the extended position on the trim and static lift, drag, and stability were generally small and within the absolute accuracy of the data, except at $M = 1.27$, where the racks caused an increment of about 0.012 in total-drag coefficient.

2. An apparently variable dynamic longitudinal stability existed when the rocket racks were extended near $M = 1.20$ and cannot be adequately explained from the results of this test; however, it is possible that it might have been the dynamic response of the model to a continuous disturbance arising from the turbulence created by the racks.

3. At subsonic Mach numbers and high lift coefficients, severe buffet probably attributable to flow separation on the wing occurred. At low supersonic Mach numbers and lift coefficients, the turbulence from the rocket racks was probably responsible for the light buffet which occurred when the racks were extended.

4. The model became statically unstable longitudinally at $M = 0.88$, $C_L = 0.60$, and pitched up, stalled, and became stable again above $C_L = 0.69$, $M = 0.85$. Subsequently the model trimmed at normal-force coefficients above 0.80.

5. At $M = 0.92$, the neutral point was at approximately 43 percent of the mean aerodynamic chord; it was at 62 percent of the mean aerodynamic chord at $M = 1.30$.

6. At $M = 0.92$, the lift curve was not a linear function of angle of attack above $C_L = 0.55$; at $M = 1.30$, it was linear within the test limits.

7. The drag due to lift was substantially reduced below $1/57.3\ C_{L_\alpha}$ by the forward tilt of the resultant force vector.

8. The static directional stability derivative C_{n_β} was approximately 0.0038 per degree at high subsonic Mach numbers.

9. The total pressure recovery of the inlet at zero mass flow varied from 75 percent at $M = 0.90$ to 65 percent at $M = 1.33$, which low values indicated the existence of a thickened boundary layer or possible boundary-layer separation on the nose cone.

10. In general, the results of the present test agree well with the results of wind-tunnel tests on similar models.

Langley Aeronautical Laboratory,
National Advisory Committee for Aeronautics,
Langley Field, Va., May 29, 1953.

Norman L. Crabill

Norman L. Crabill
Aeronautical Research Scientist

Approved: Joseph A. Shortal
Joseph A. Shortal
Chief of Pilotless Aircraft Research Division

lrf

APPENDIX

METHODS OF ACCOUNTING FOR EFFECTS OF RACKS

The wind-tunnel data were adjusted to a center-of-gravity location of 28.5 percent of the mean aerodynamic chord and a stabilizer deflection of -5.91° by conventional methods. The effect of partially opened racks on the trim was allowed for in two ways:

(a) The change in $C_{m_{(C_L=0)}}$ was calculated from

$$\Delta C_{m_{(C_L=0)_{(\delta_{RR})}}} = \Delta C_{m_{(C_L=0)_{(\delta_{RR}=114.3^\circ)}}} \frac{(S_{RR}\,l)_{(\delta_{RR})}}{(S_{RR}\,l)_{(\delta_{RR}=114.3^\circ)}} \tag{1}$$

(b) The small change in stability with rack position shown in reference 4 was disregarded when the racks were less than half open. When more than half open, the full amount of the shift was assumed.

The increment in α_{trim} due to the design extension of the rocket racks, shown in figure 12, was computed from

$$\Delta\alpha_{trim_{(\delta_{RR}=114.3^\circ)}} = \frac{\alpha_{trim_{(\delta=122^\circ)}} - \alpha_{trim_{(\delta<122^\circ)}}}{\dfrac{(S_{RR}\,l)_{(\delta=122^\circ)} - (S_{RR}\,l)_{(\delta<122^\circ)}}{(S_{RR}\,l)_{(\delta=114.3^\circ)}}} \tag{2}$$

The increment in drag coefficient due to the design extension of the rocket racks was estimated from the measured increment in drag coefficient caused by the racks moving from slightly more than fully open to partially closed by

$$\Delta C_{D_{(\delta_{RR}=114.3^\circ)}} = \frac{\left[C_{D_{(\delta=122^\circ)}} - C_{D_{(\delta<122^\circ)}}\right]_{(C_L=\text{Constant})}}{\dfrac{S_{RR_{(\delta=122^\circ)}} - S_{RR_{(\delta<122^\circ)}}}{S_{RR_{(\delta=114.3^\circ)}}}} \tag{3}$$

REFERENCES

1. Gillis, Clarence L., Peck, Robert F., and Vitale, A. James: Preliminary Results From a Free-Flight Investigation at Transonic and Supersonic Speeds of the Longitudinal Stability and Control Characteristics of an Airplane Configuration With a Thin Straight Wing of Aspect Ratio 3. NACA RM L9K25a, 1950.

2. Morrow, John D., and Nelson, Robert L.: Large-Scale Flight Measurements of Zero-Lift Drag of 10 Wing-Body Configurations at Mach Numbers From 0.8 to 1.6. NACA RM L52D18a, 1952.

3. Krenkel, A. R.: Model XF3H-1 - Supersonic Wind Tunnel Tests at 0.A.L. on 1.5% and 4.5% Scale Models. Rep. No. 1685 (Contract NOa(s)-10260), McDonnell Aircraft Corp., May 19, 1950.

4. Rousseau, W. A.: Model XF3H-1 - Basic Wind Tunnel Longitudinal Stability Data - Mach Nos. .18 Thru 1.73. Rep. No. 2101 (Contract NOa(s)-10260), McDonnell Aircraft Corp., May 15, 1951.

5. Cunningham, H. J.: Analysis of Pure-Bending Flutter of a Cantilever Swept Wing and Its Relation to Bending-Torsion Flutter. NACA TN 2461, 1951.

6. Sohn, R. F., Grose, G. G., Allen, D. W., Lacey, T. R., and Gillooly, R. P.: Model XF3H-1 - Analysis of Preliminary Flight Test Results - Revision Number 1. Rep. No. 2496 (Contract NOa(s)-10260), McDonnell Aircraft Corp., Aug. 29, 1952.

7. Von Tungeln, F. W.: Report on High-Speed Wind Tunnel Tests of a 0.10-Scale Model of the McDonnell XF3H-1 Airplane. CWT Rep. 152, Southern Calif. Cooperative Wind Tunnel, Nov. 3, 1950.

8. Pliske, D. R.: Model XF3H-1 - Summary of Transonic Wind Tunnel Tests on a 2% Scale Bump Model - Series I. Rep. No. 1545 (Contract NOa(s)-10260), McDonnell Aircraft Corp., Mar. 1, 1950.

9. Carter, Howard S., and Merlet, Charles F.: Flight Determination of the Pressure Recovery and Drag Characteristics of a Twin Side-Inlet Model at Transonic Speeds. NACA RM L53E05, 1953.

10. Vitale, A. James: Effects of Wing Elasticity on the Aerodynamic Characteristics of an Airplane Configuration Having 45° Sweptback Wings As Obtained From Free-Flight Rocket-Model Tests at Transonic Speeds. NACA RM L52L30, 1953.

11. Gillis, Clarence L., and Chapman, Rowe, Jr.: Summary of Pitch-Damping Derivatives of Complete Airplane and Missile Configurations As Measured in Flight at Transonic and Supersonic Speeds. NACA RM L52K20, 1953.

12. Bishop, Robert C., and Lomax, Harvard: A Simplified Method for Determining From Flight Data the Rate of Change of Yawing-Moment Coefficient With Sideslip. NACA TN 1076, 1946.

13. Clark, D. D.: Model XF3H-1 - Summary of Preliminary Lateral-Directional Dynamic Stability Calculations. Rep. No. 1544 (Contract NOa(s)-10260), McDonnell Aircraft Corp., Jan. 20, 1950.

TABLE I

PERTINENT PHYSICAL PROPERTIES AND DIMENSIONS

	Wing	Stabilizer	Fin
Dimensions:			
Span, in.	42.40	17.40	8.55
Mean aerodynamic chord, in.	14.63	6.00	7.93
Area, total, sq ft	4.15	0.750	0.454
Aspect ratio	3	3	1.118
Taper ratio	0.5	0.5	0.5
Incidence, deg	[1]2.00	[2]-5.91	[1]0.23
Twist, deg	0	0	0
Dihedral, deg	0	0	-----
Airfoil section at -			
Root	NACA 0009-1.16 38/1.14 mod.	NACA 0007-1.16 38/1.14 mod.	
Tip	NACA 0007-1.16 38/1.14 mod.		
Sweepback of c/4 line, deg	45	45	45
Location of c/4 point of MAC:			
Longitudinal, fuselage station, in.	32.97	63.36	60.93
Vertical, distance from bottom of fuselage, in.	2.52	7.60	12.59
Lateral, spanwise distance from fuselage center line, in.	9.38	3.81	0
Fuselage base area, sq ft	0.0767		

[1]Relative to fuselage center line

[2]Relative to wing chord plane

Mass characteristics:	
Weight, lb	120.49
Wing loading, lb/sq ft	29.03
Center-of-gravity location:	
Longitudinal, percent M.A.C. behind L.E.	28.5
Vertical, percent M.A.C. above center line	1.2
Lateral, percent M.A.C. right of center line	0.4
Moments of inertia about the principal axes:	
I_X, slug-ft^2	0.96
I_Y, slug-ft^2	5.36
I_Z, slug-ft^2	6.03
Inclination of the principal X-axis at the nose below the fuselage center line, deg	2.90

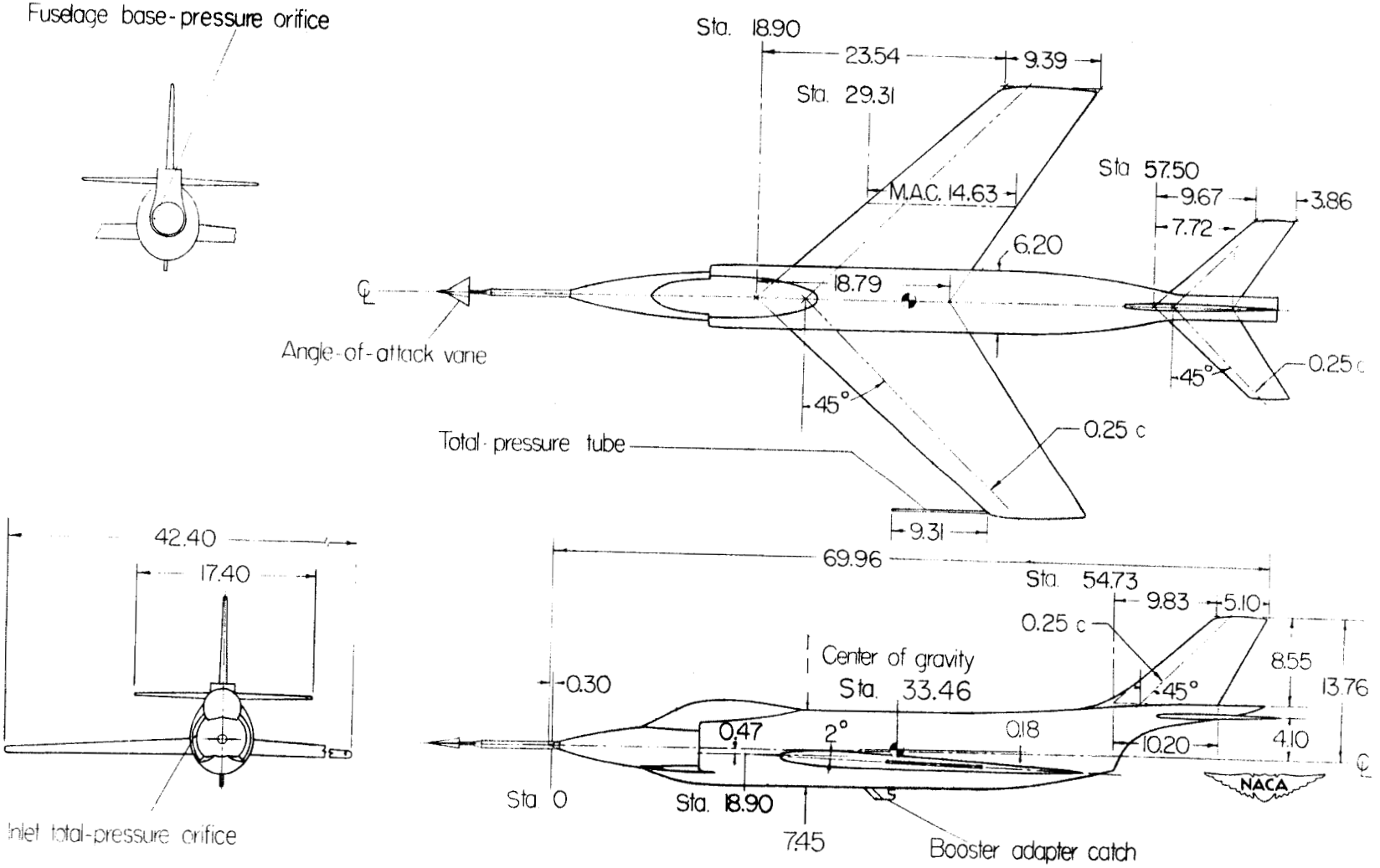

Figure 1.- General arrangement of the 1/10-scale model of the McDonnell XF3H-1 airplane. All dimensions are in inches.

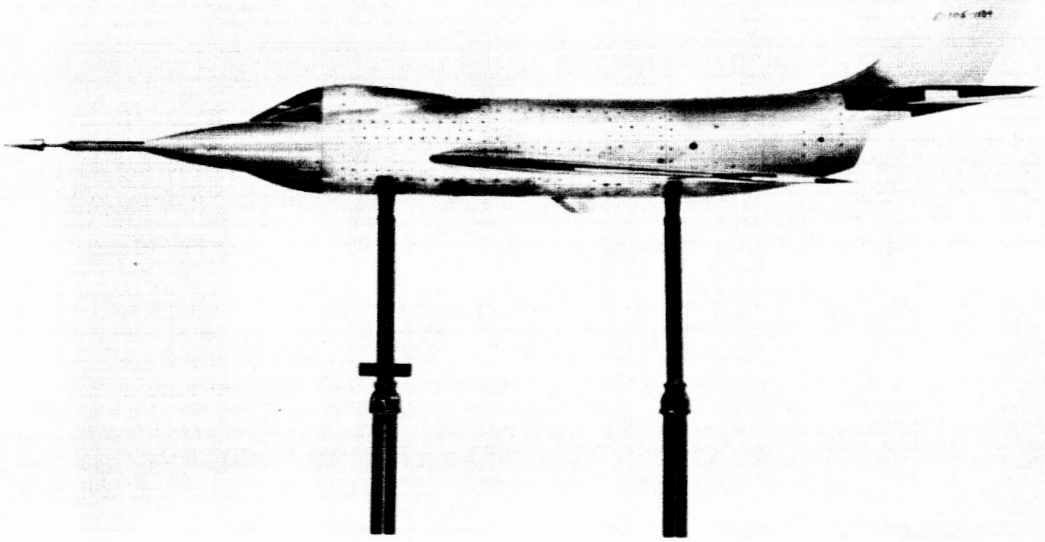

NACA L-74321

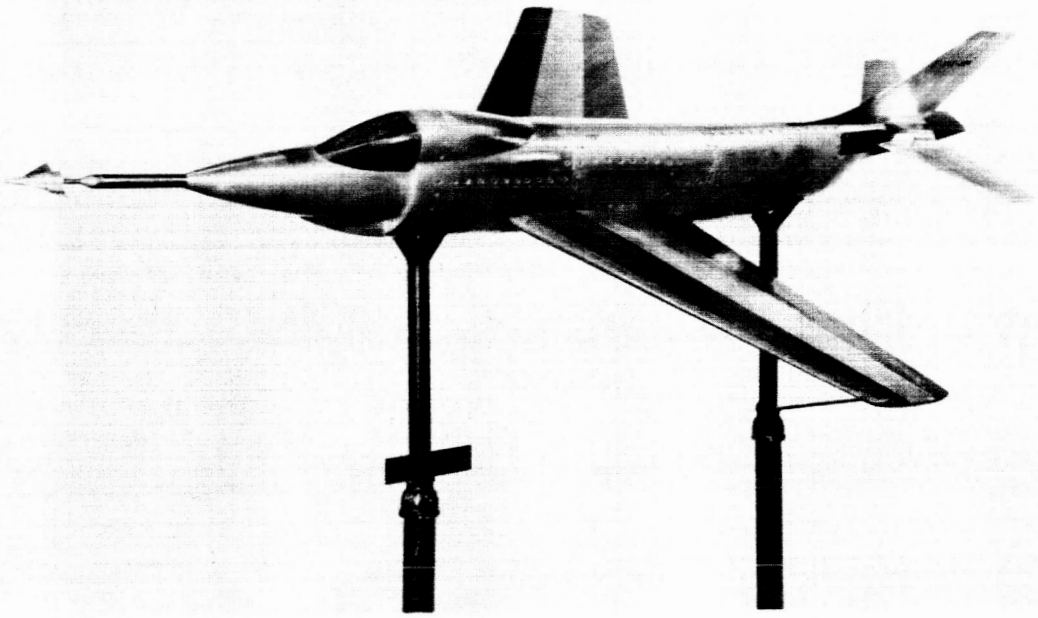

Figure 2.- Model photographs.

NACA L-74319

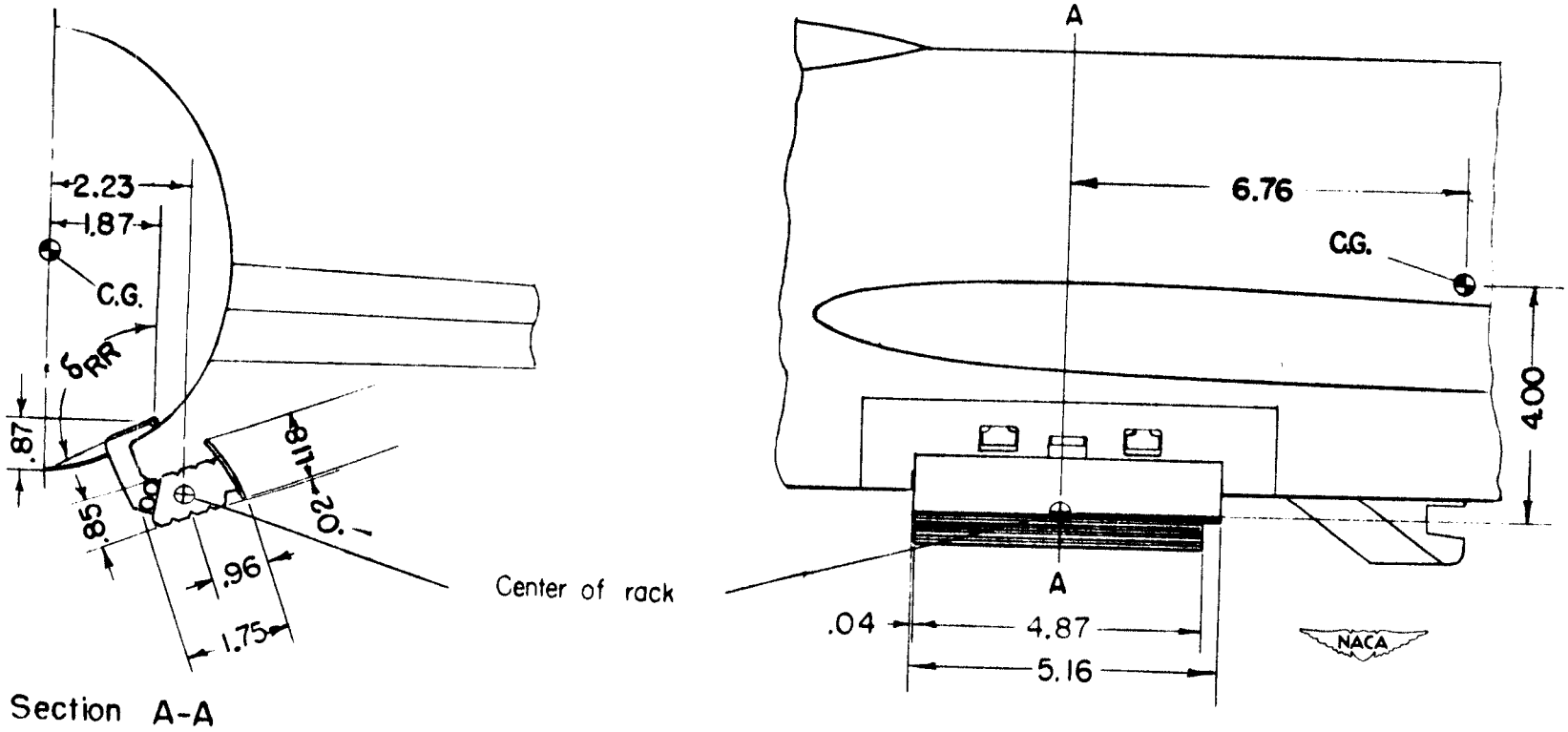

Rocket – Rack Design Conditions

Position	Extension	Frontal area
Closed	0	0
Open	114.3°	0.022 ft^2

Figure 3.- Rocket-rack configuration. All dimensions are in inches.

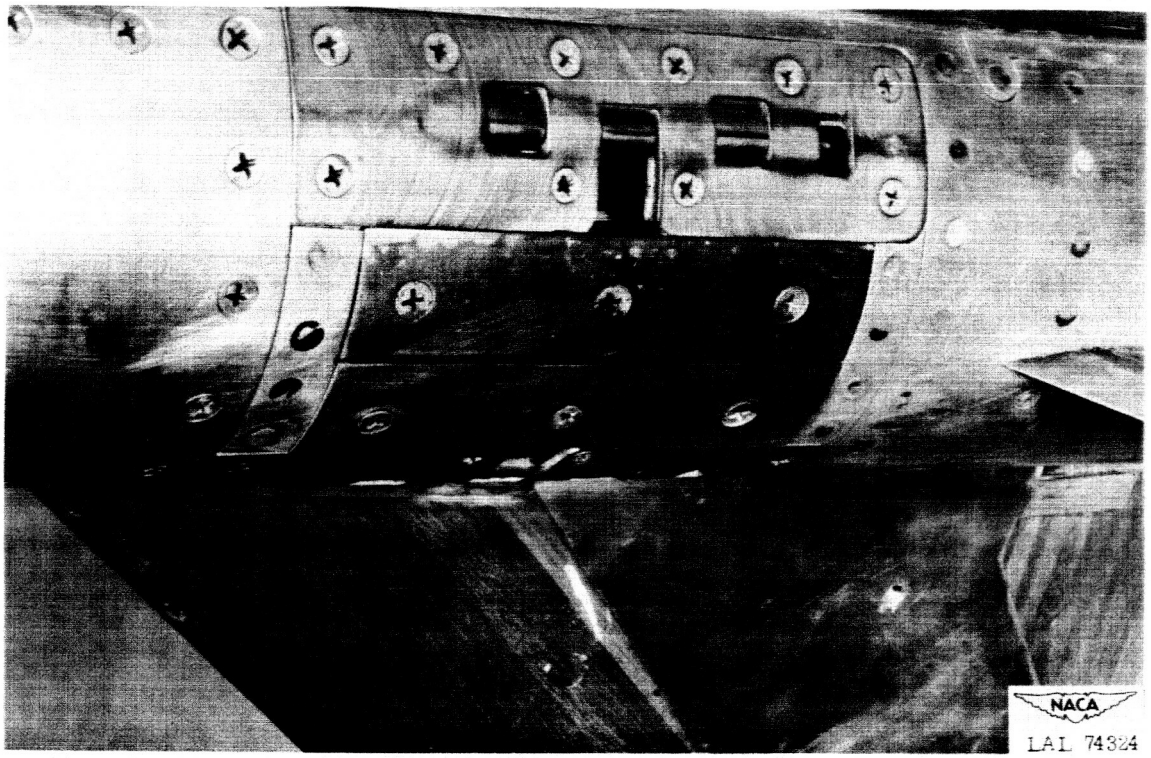

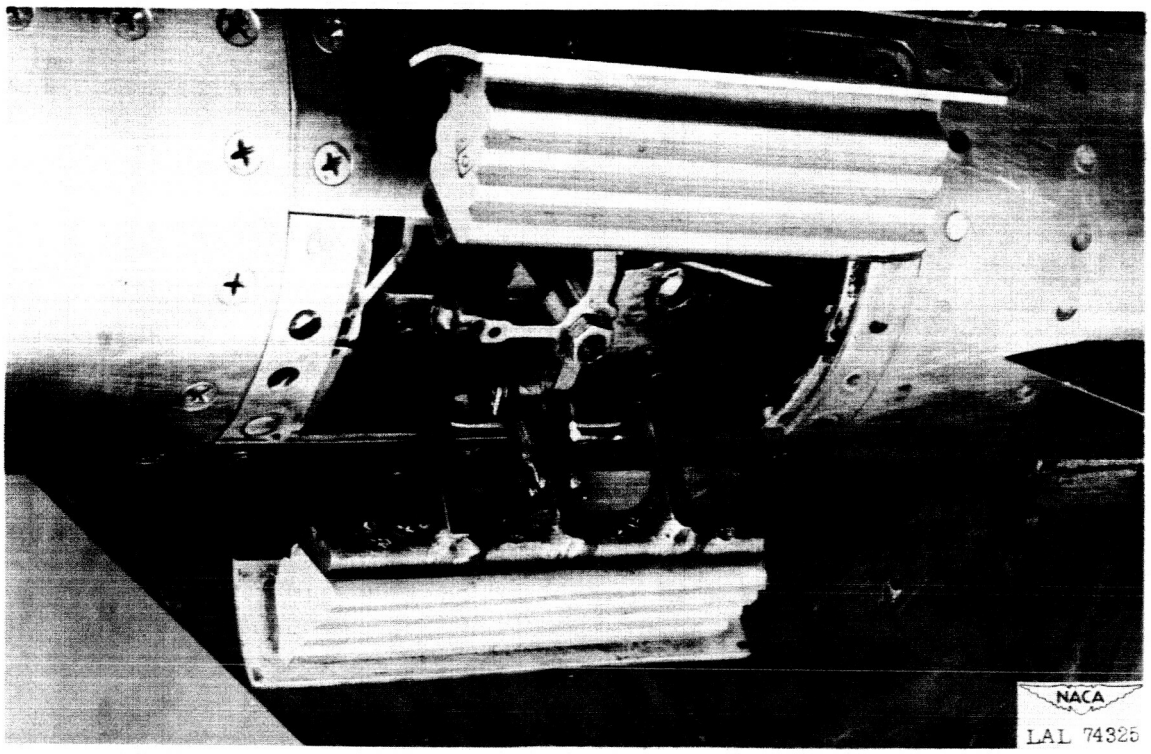

Figure 4.- Photographs of the rocket racks. Closed and open.

Resonant frequencies, cycles per second
When mechanically shaken: as noted on node lines
When struck:

Wing	87
Stabilizer	88,115
Fin	97

Node lines
— — X — — indicates node line occurring when model was continuosly shaken at X cps

Accelerometer locations
A, normal at C.G.
B, normal at tail
C, chordwise
D, transverse

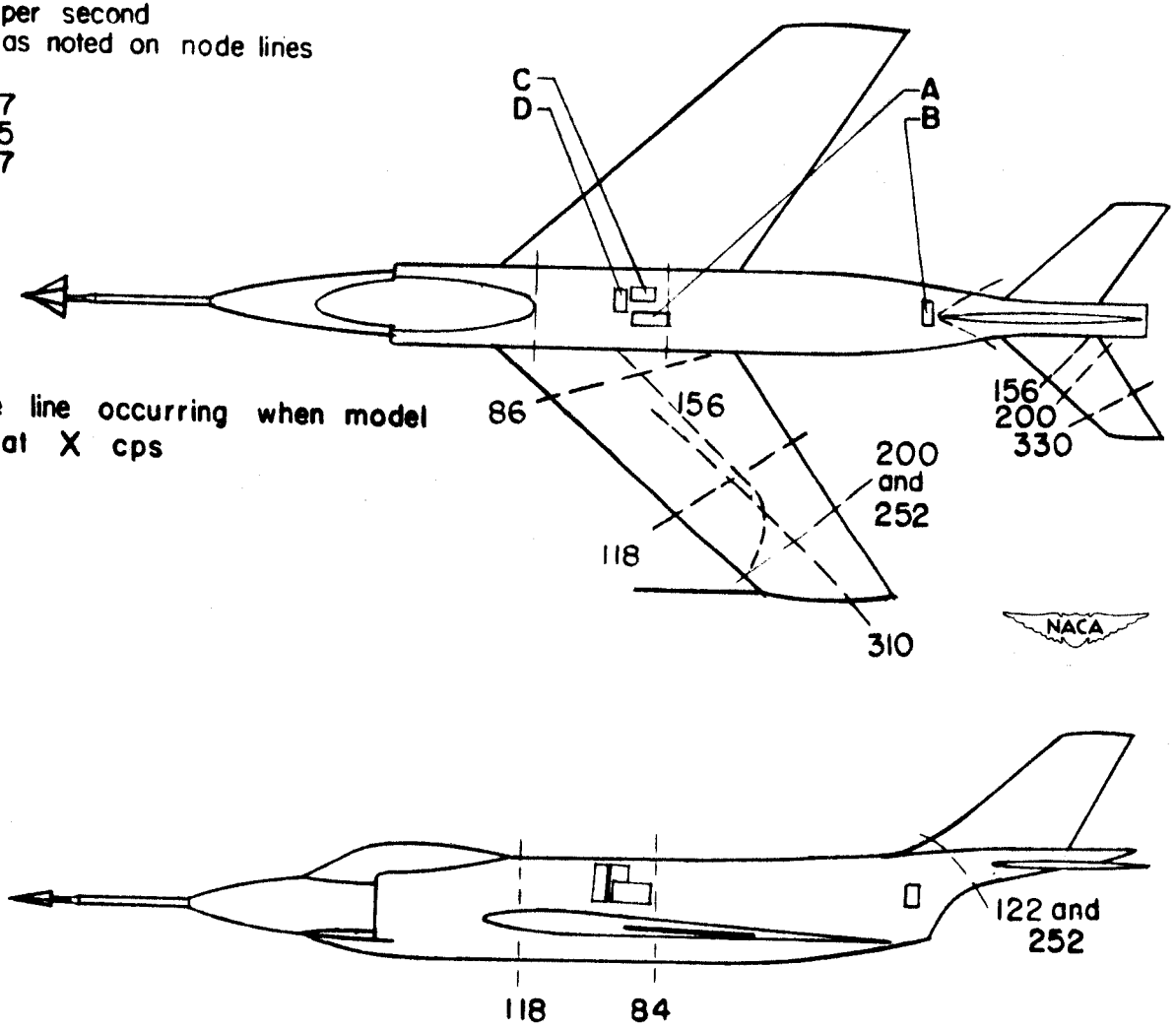

Figure 5.- Resonant frequencies, node lines, and accelerometer locations.

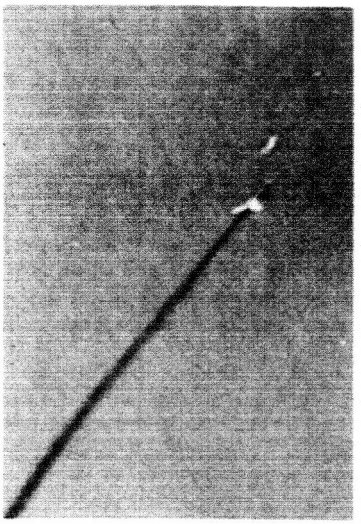

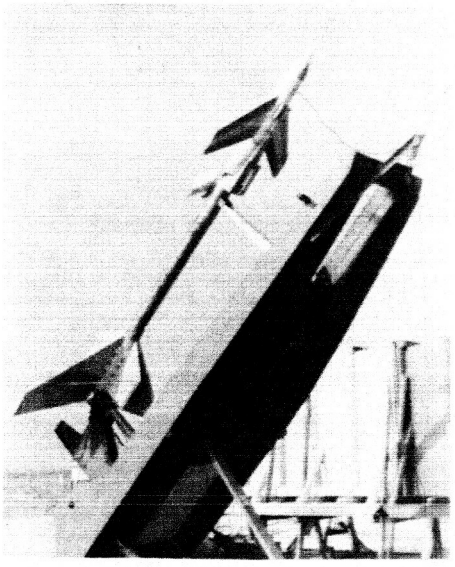

Figure 6.- Photographs of the model before launching and just after separation.

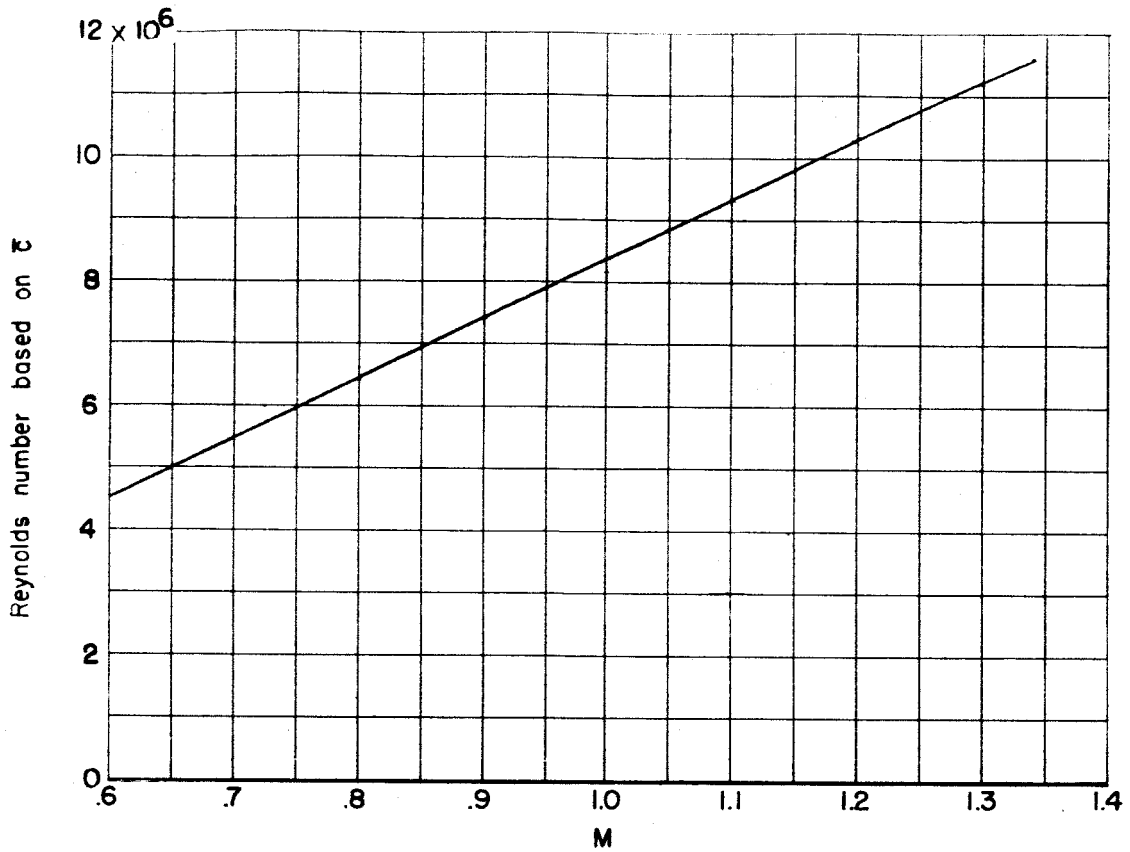

Figure 7.- Test Reynolds number as a function of Mach number.

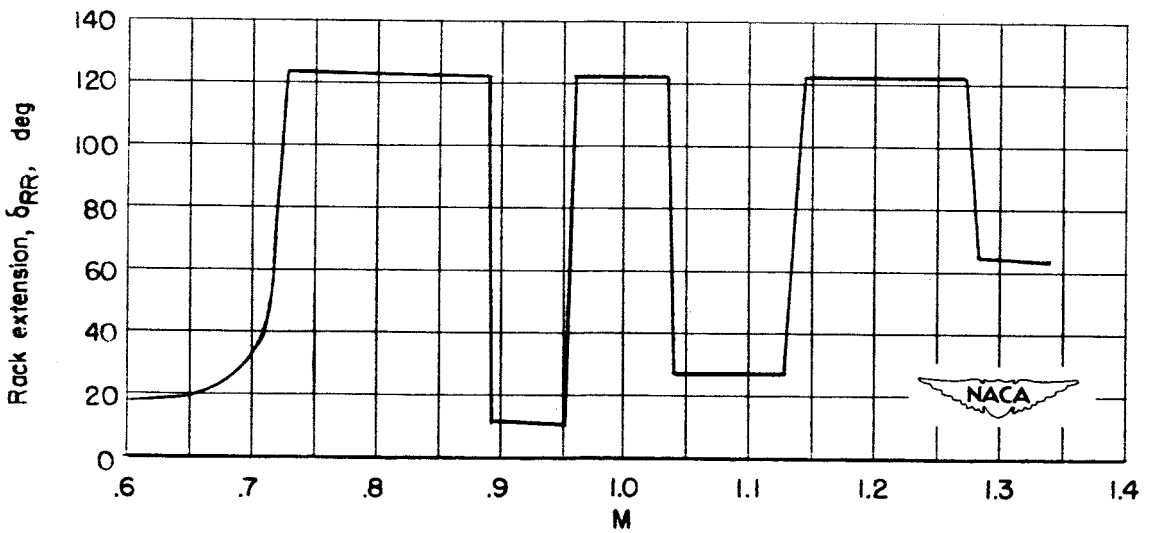

Figure 8.- Rocket-rack position as a function of Mach number.

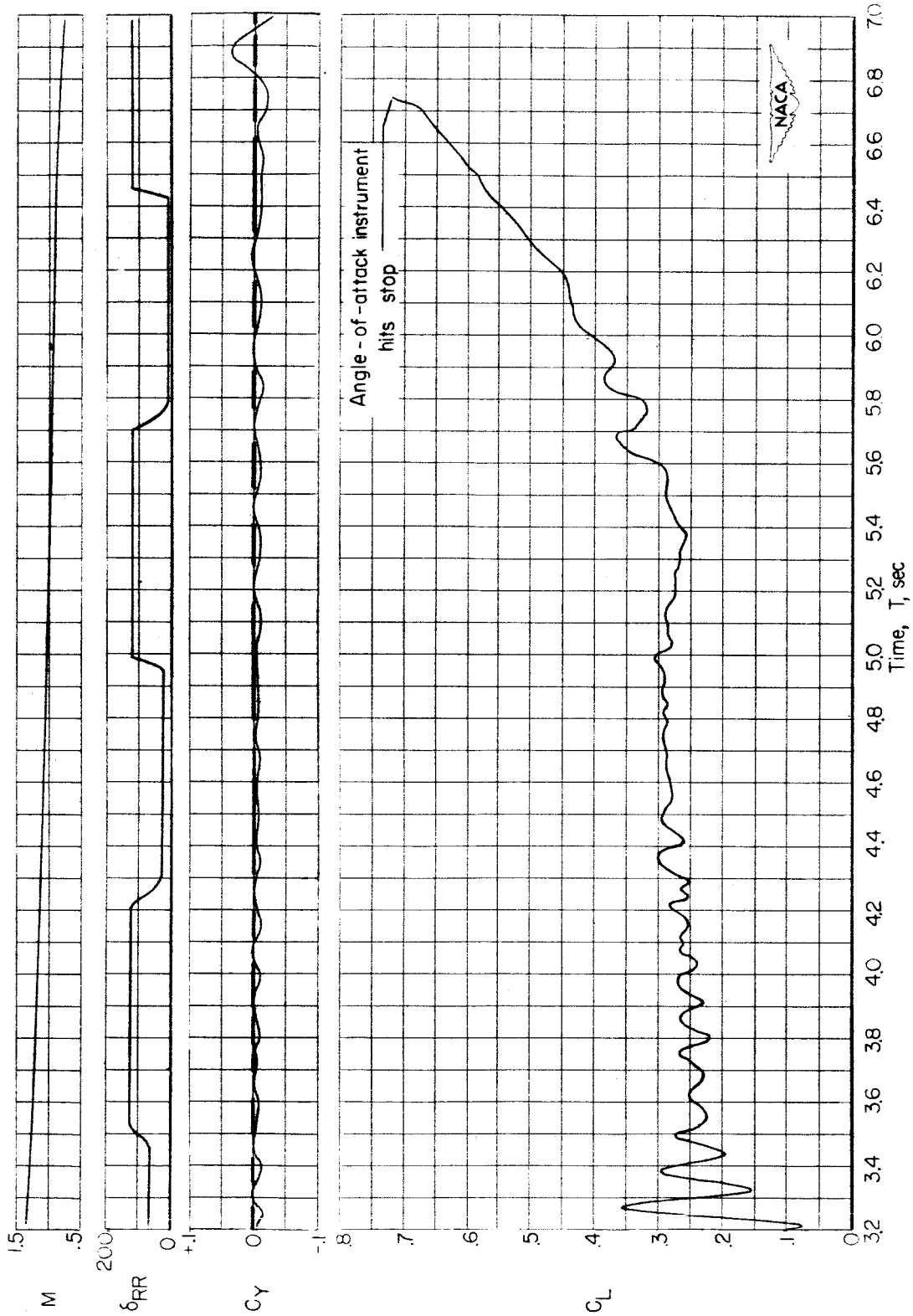

Figure 9.- Partial time history.

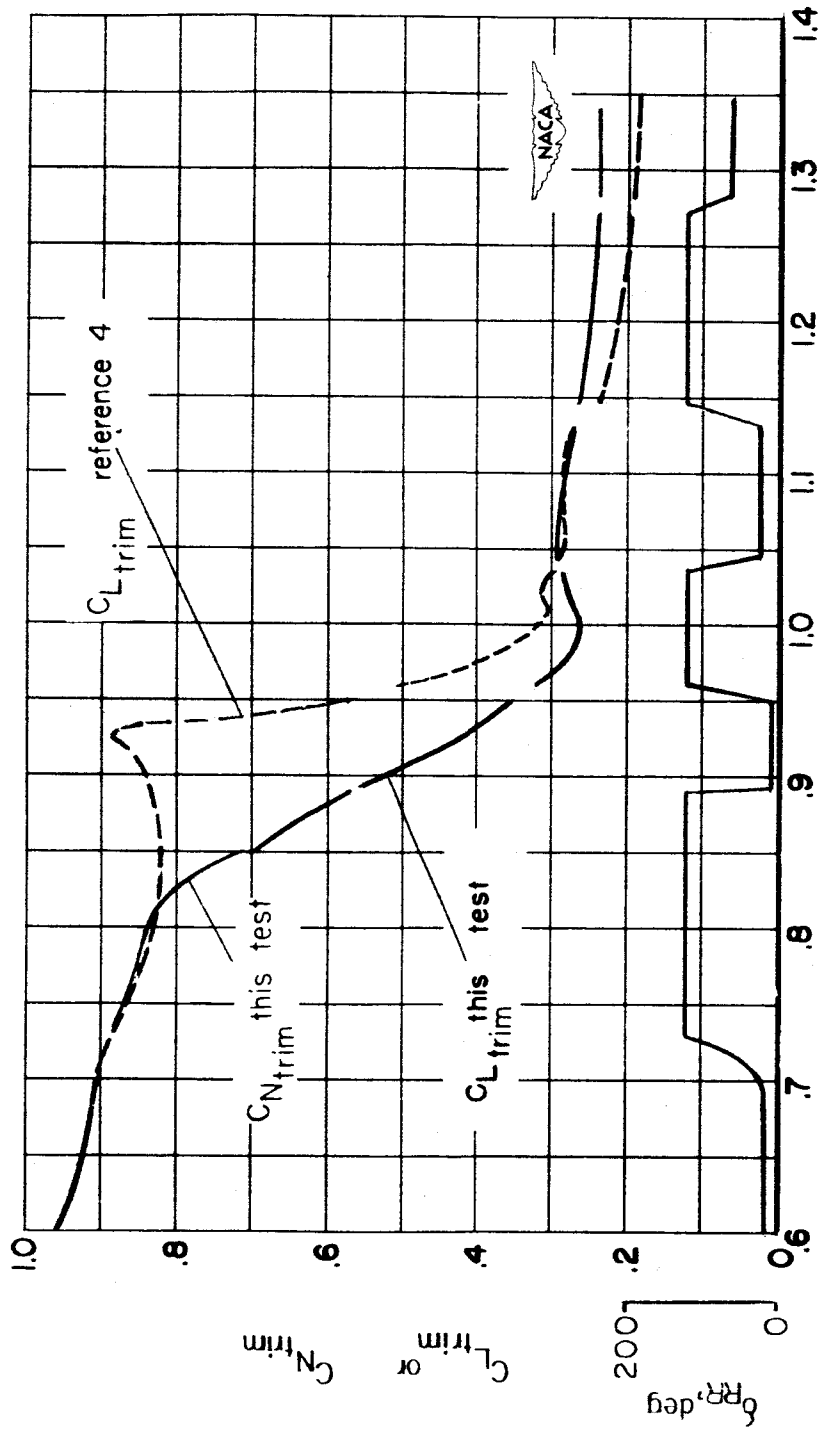

Figure 10.- Trim lift coefficient.

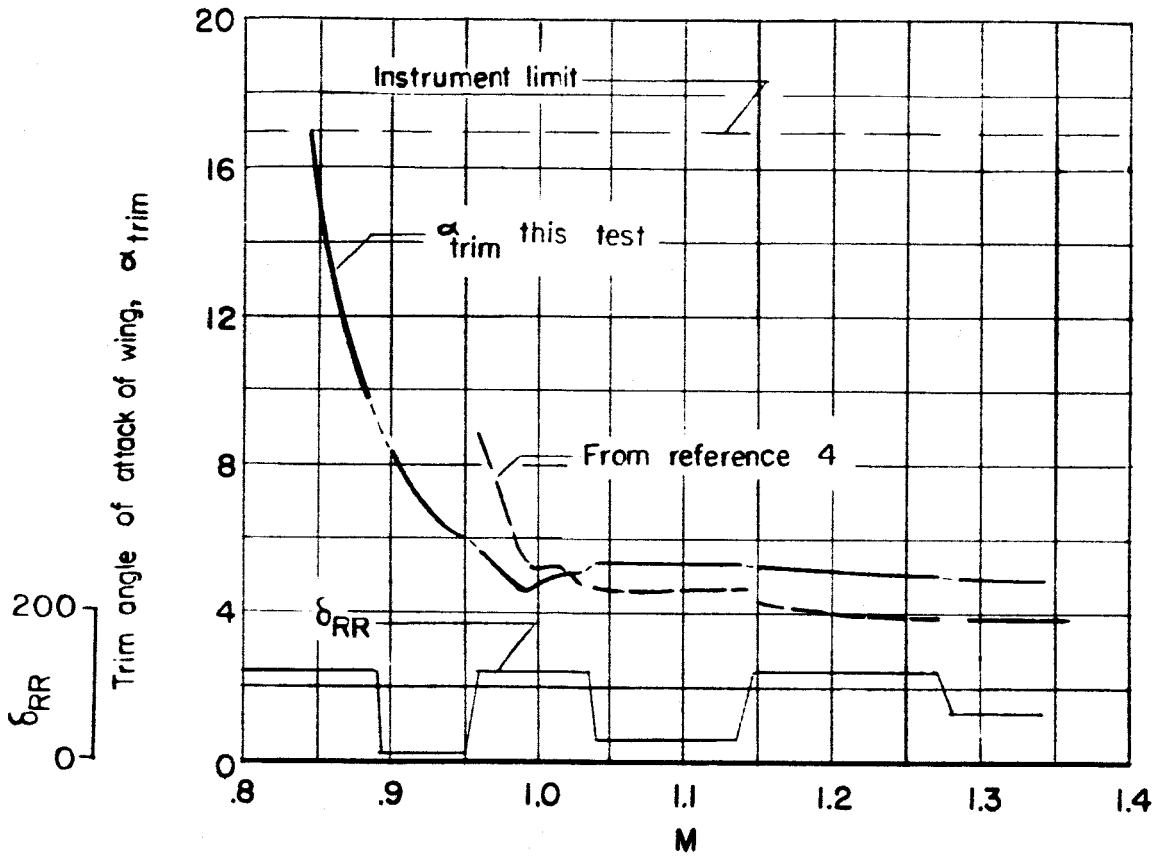

Figure 11.- Wing-chord-plane angle of attack.

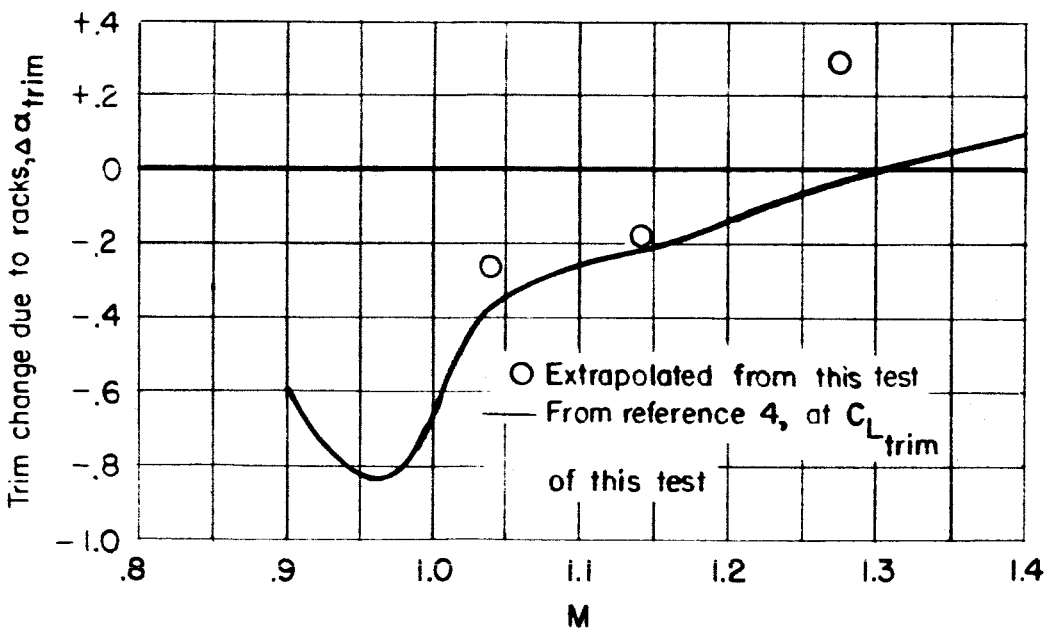

Figure 12.- Increment in trim angle of attack for $\delta_{RR} = 114.3^{\circ}$.

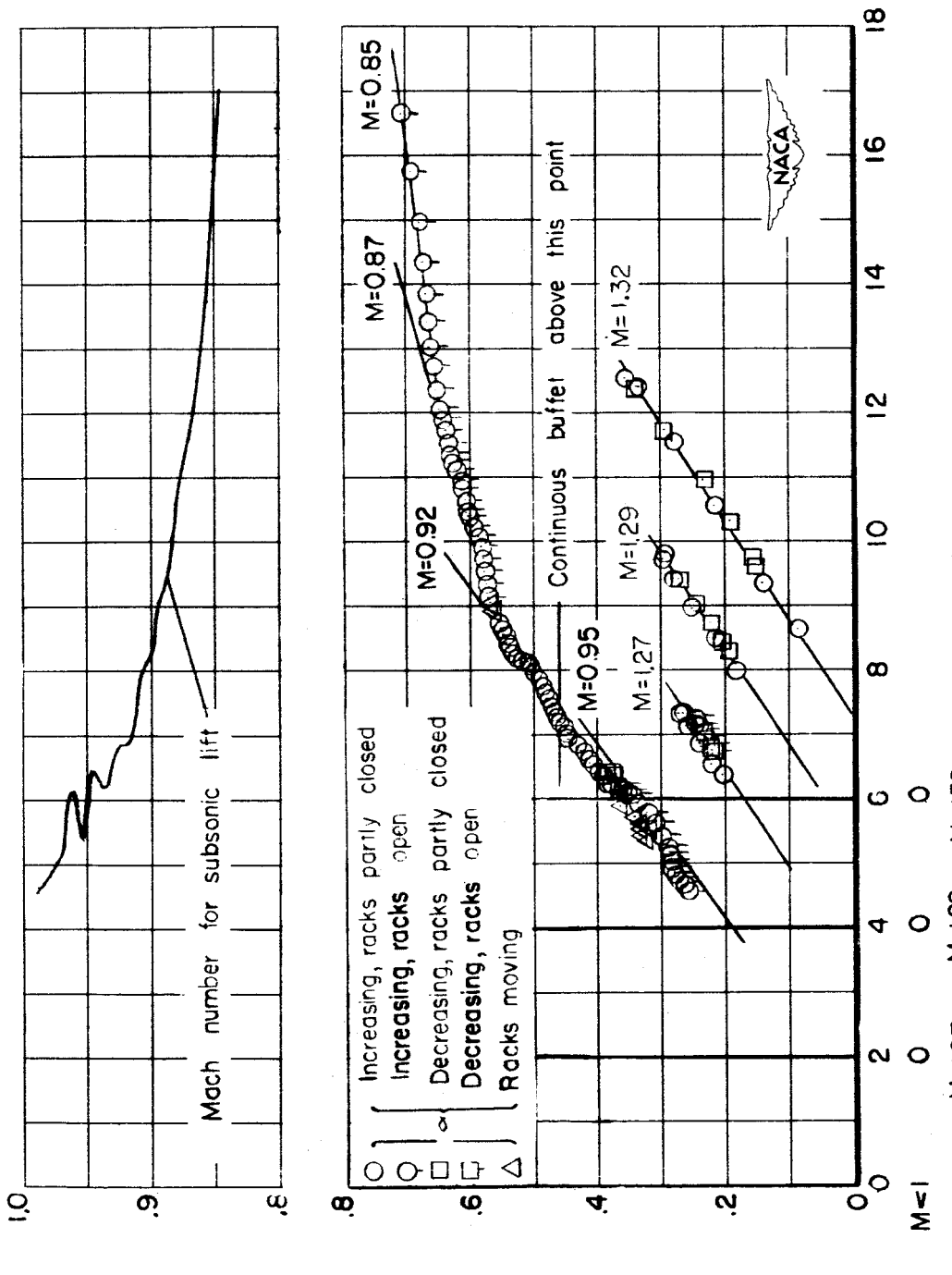

Figure 13.- Lift coefficient as a function of wing angle of attack.

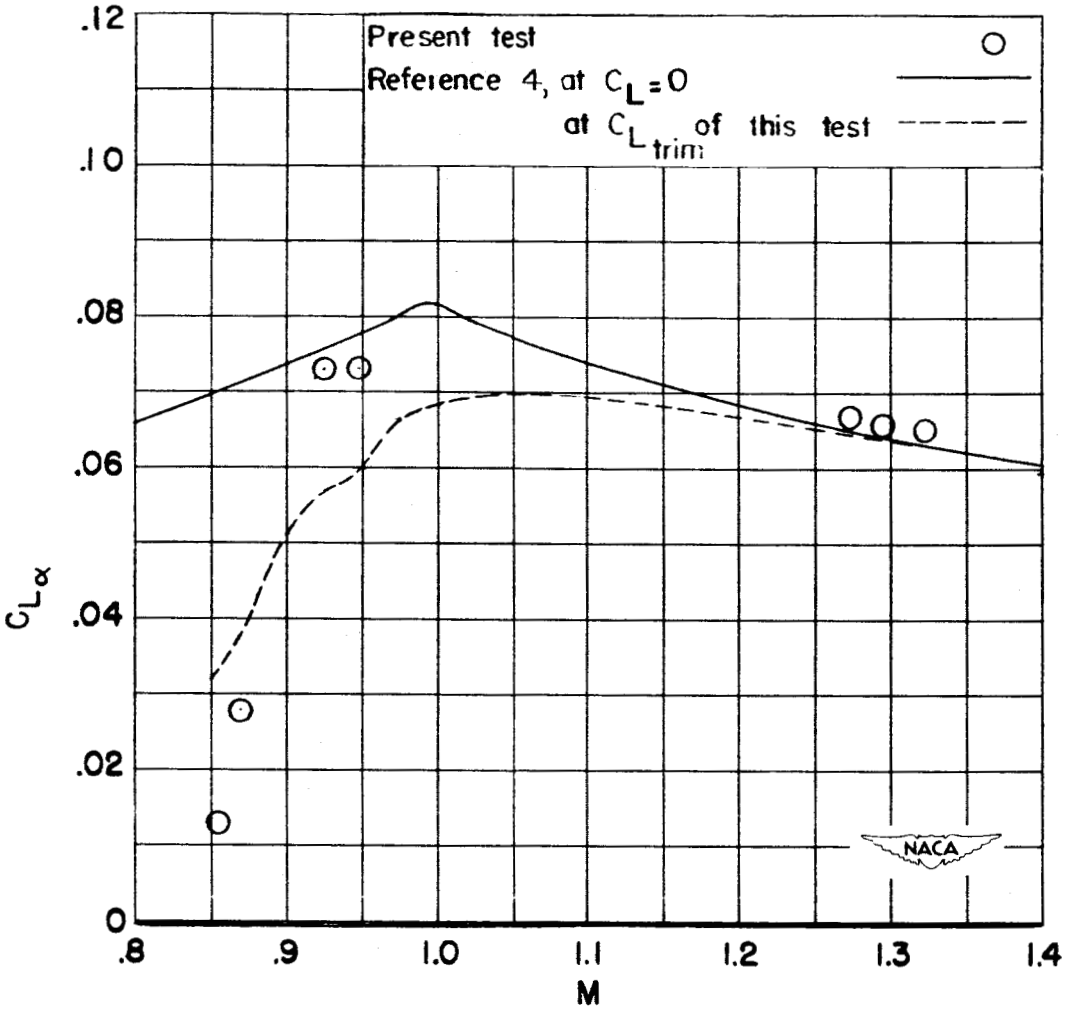

Figure 14.- Lift-curve slope.

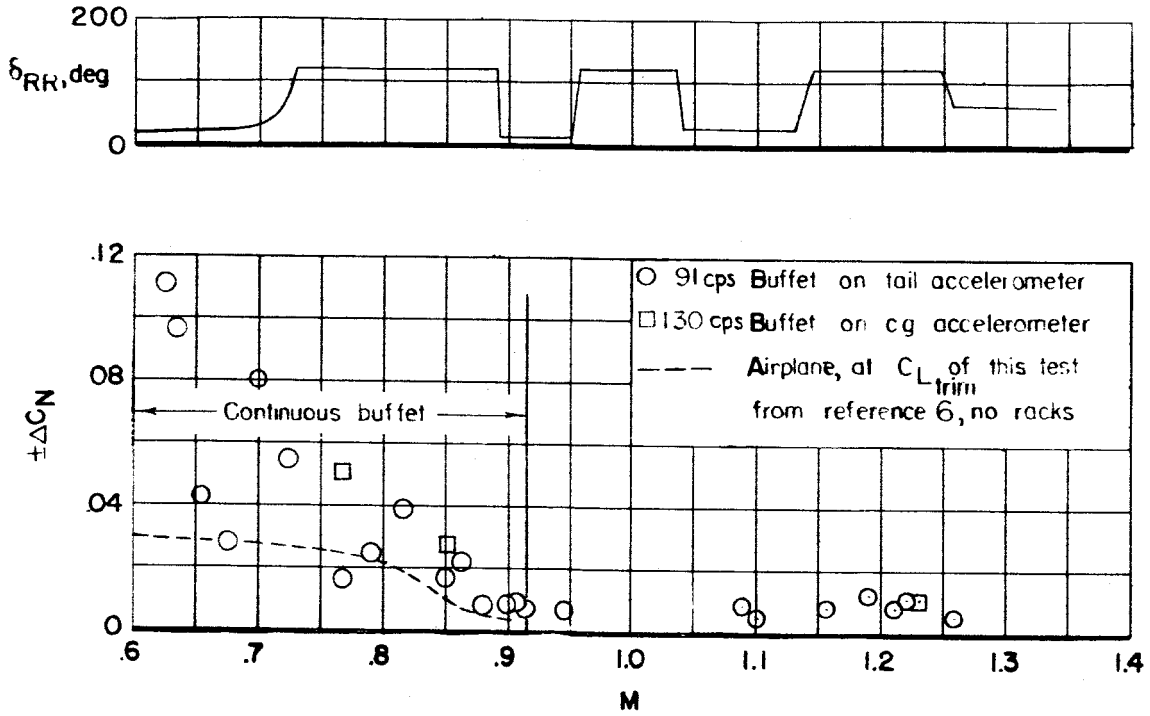

Figure 15.- Buffet amplitudes observed on the normal accelerometers near $C_{L_{trim}}$.

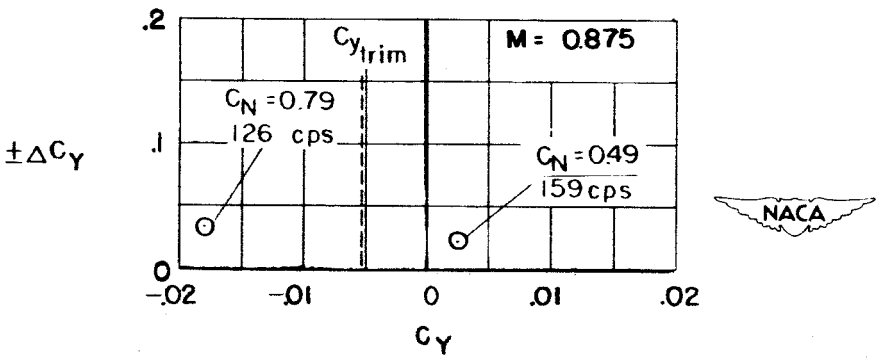

Figure 16.- Buffet amplitudes observed on the lateral accelerometer.

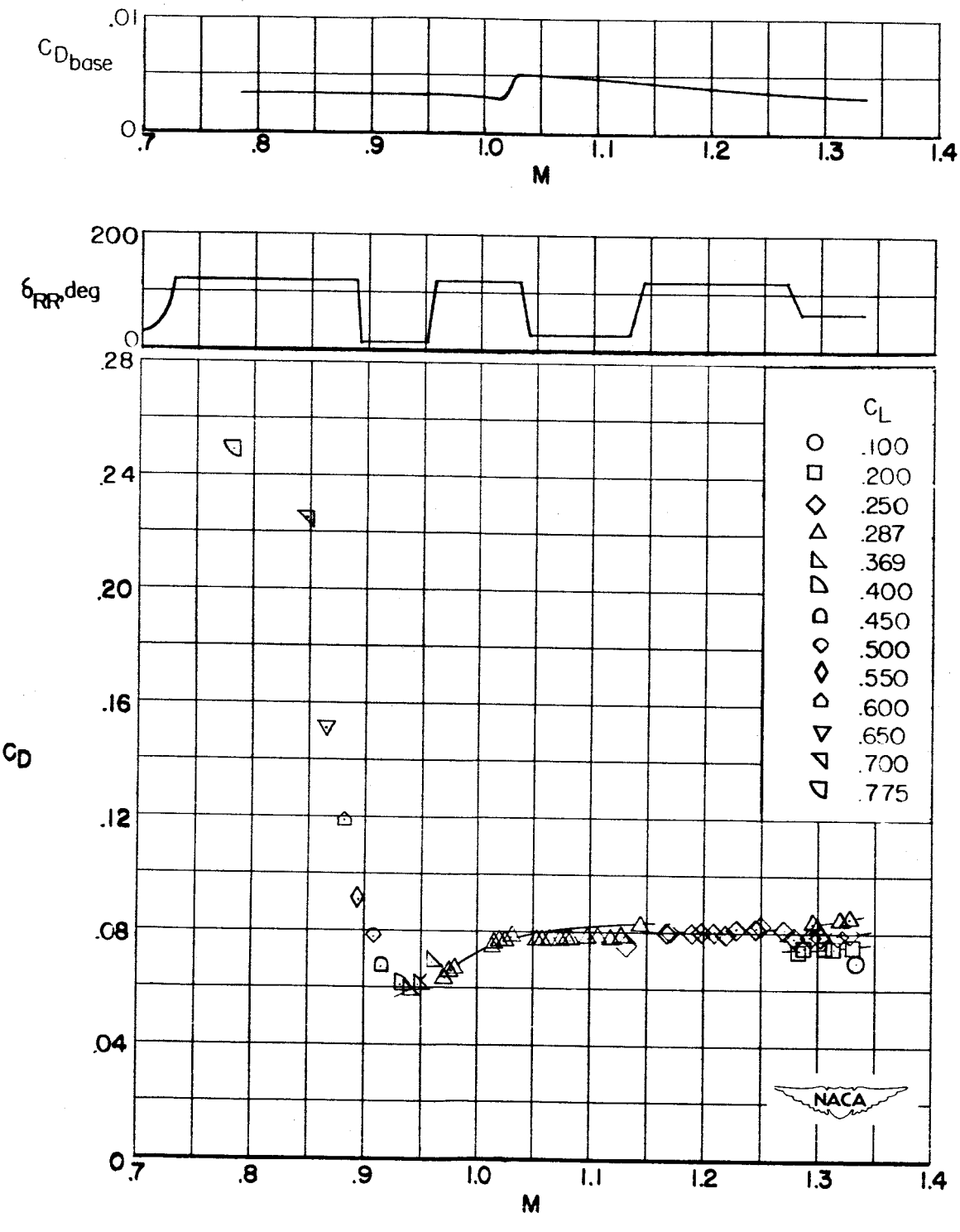

Figure 17.- Drag carpet and base-drag coefficient.

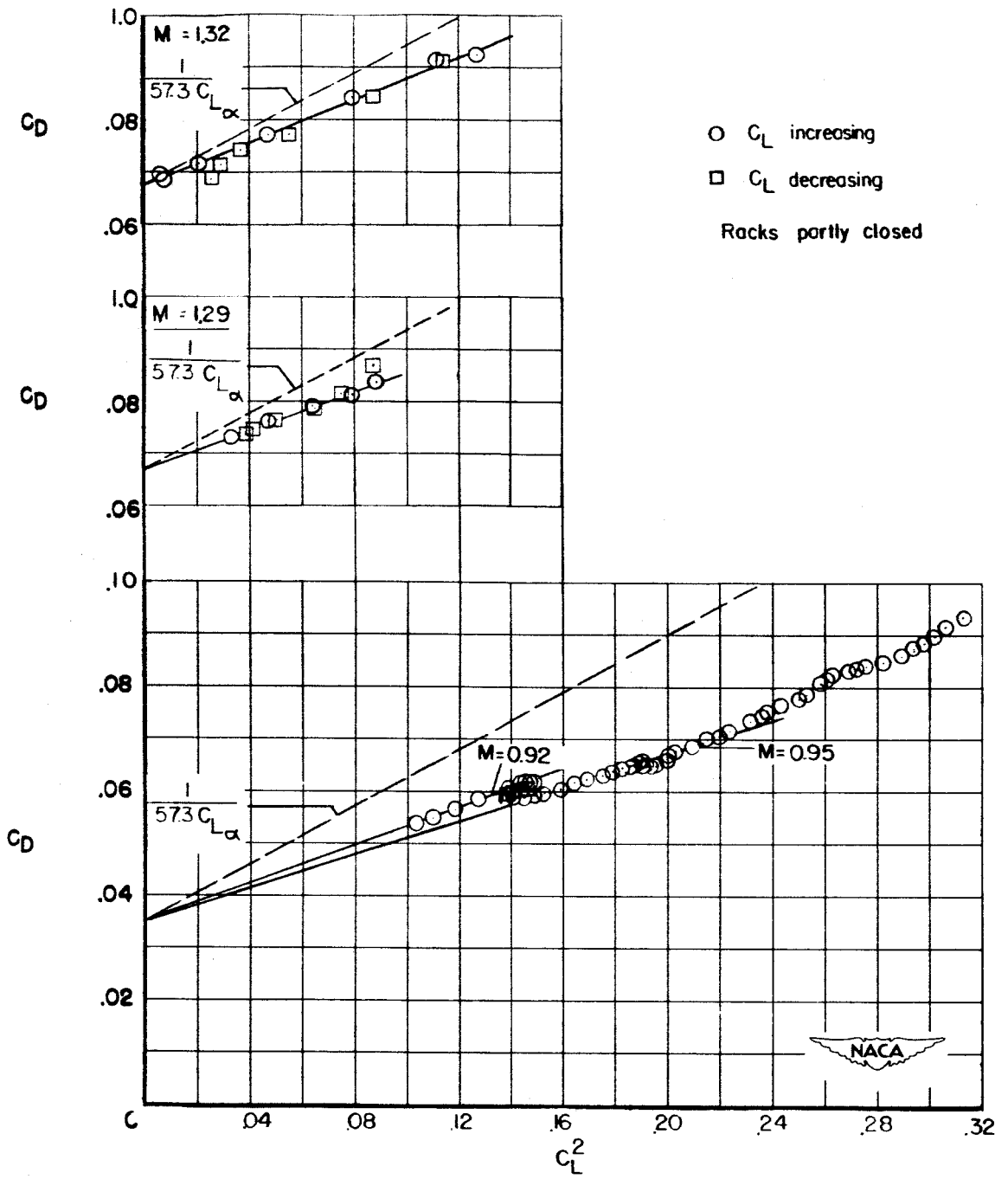

Figure 18.- Variation of total-drag coefficient with the square of the total-lift coefficient at several Mach numbers.

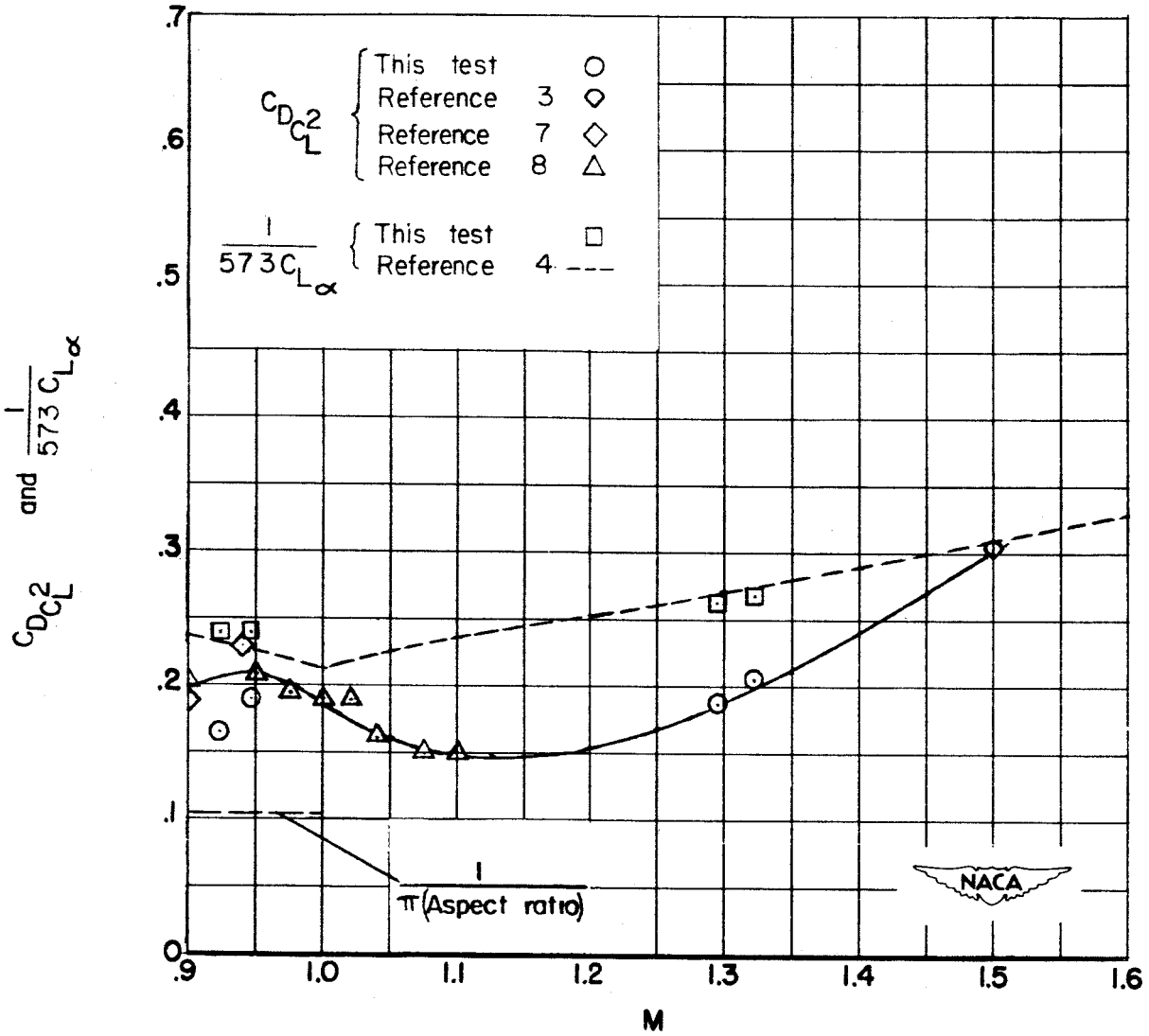

Figure 19.- Variation of drag with lift.

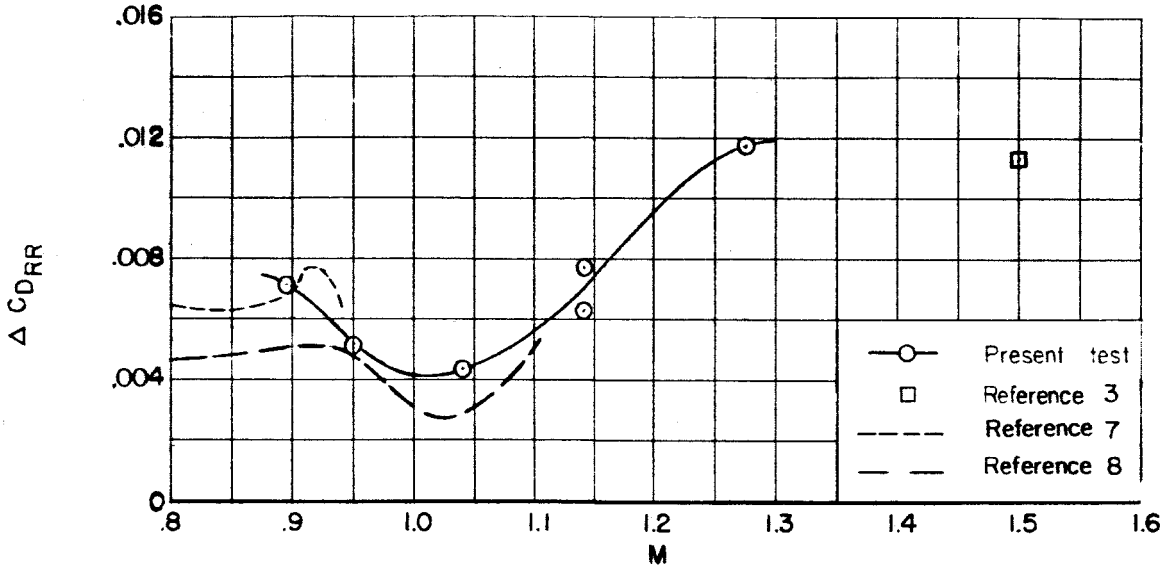

Figure 20.- Increment in drag coefficient due to the presence of the rocket racks.

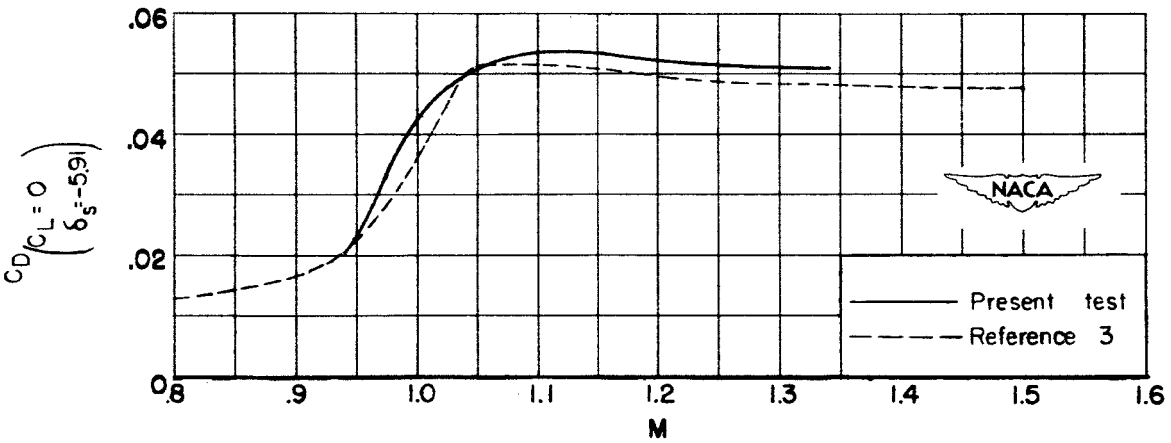

Figure 21.- Minimum drag coefficient as a function of Mach number.

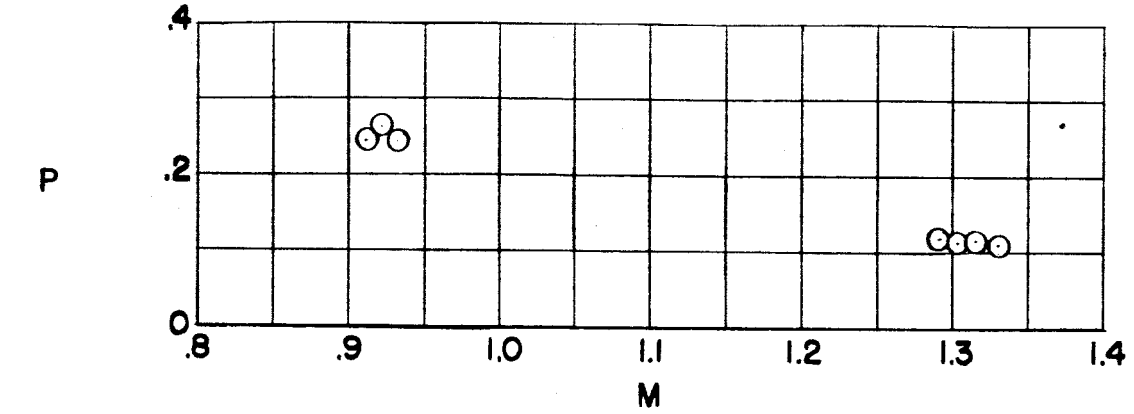

(a) Longitudinal period.

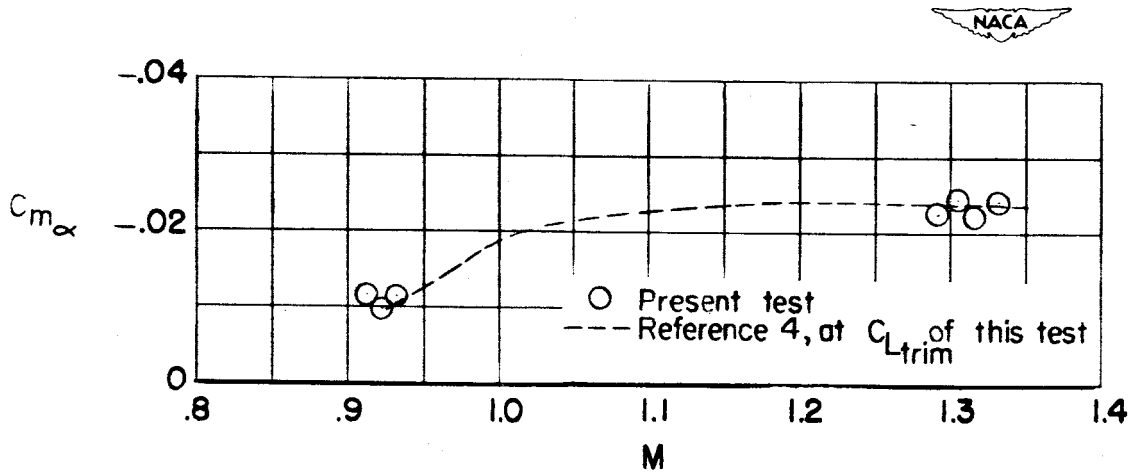

(b) Longitudinal static stability derivative C_{m_α}.

Figure 22.- Longitudinal static stability parameters.

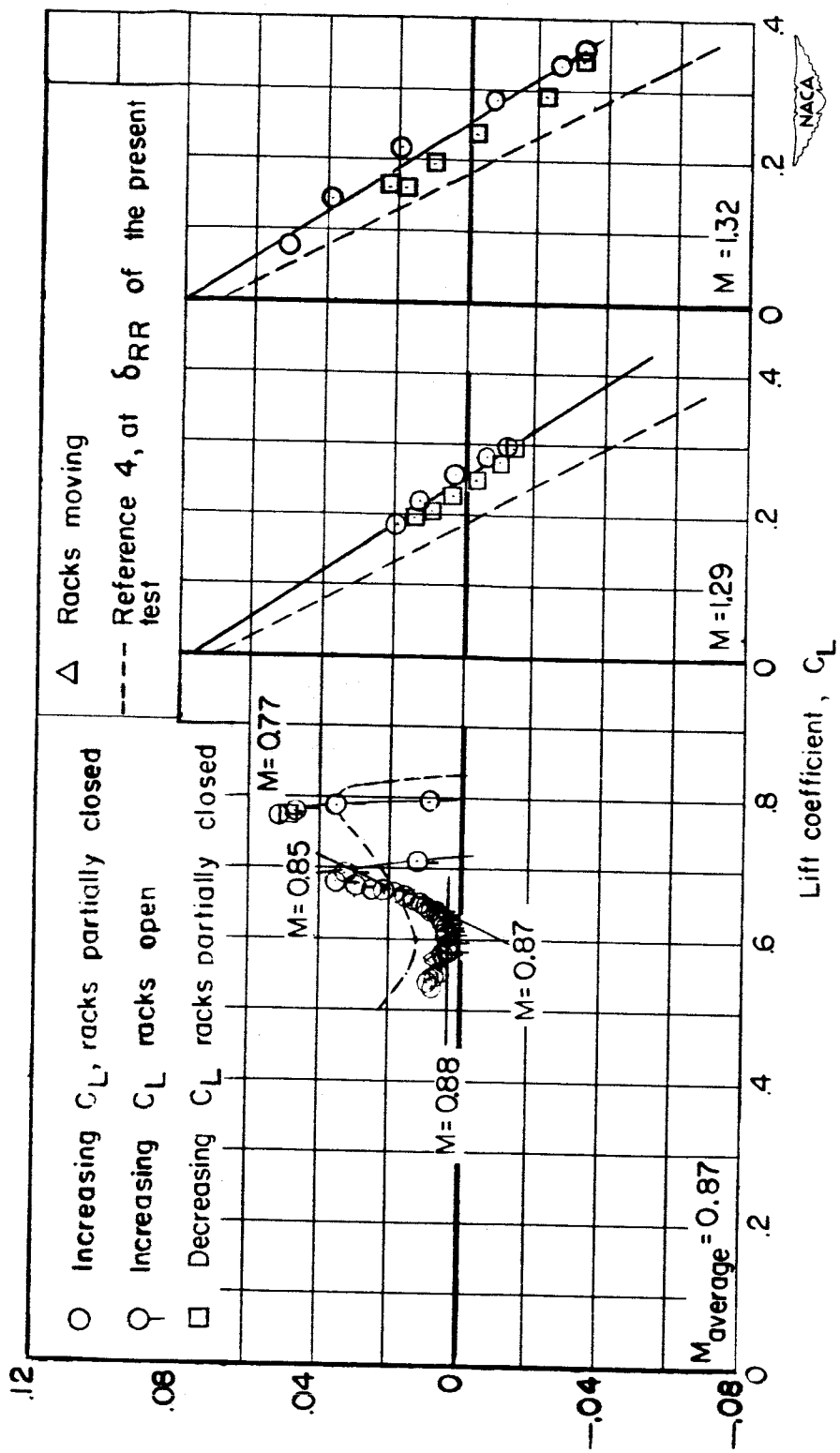

Figure 23.- Static pitching moment coefficient as a function of lift coefficient at several Mach numbers.

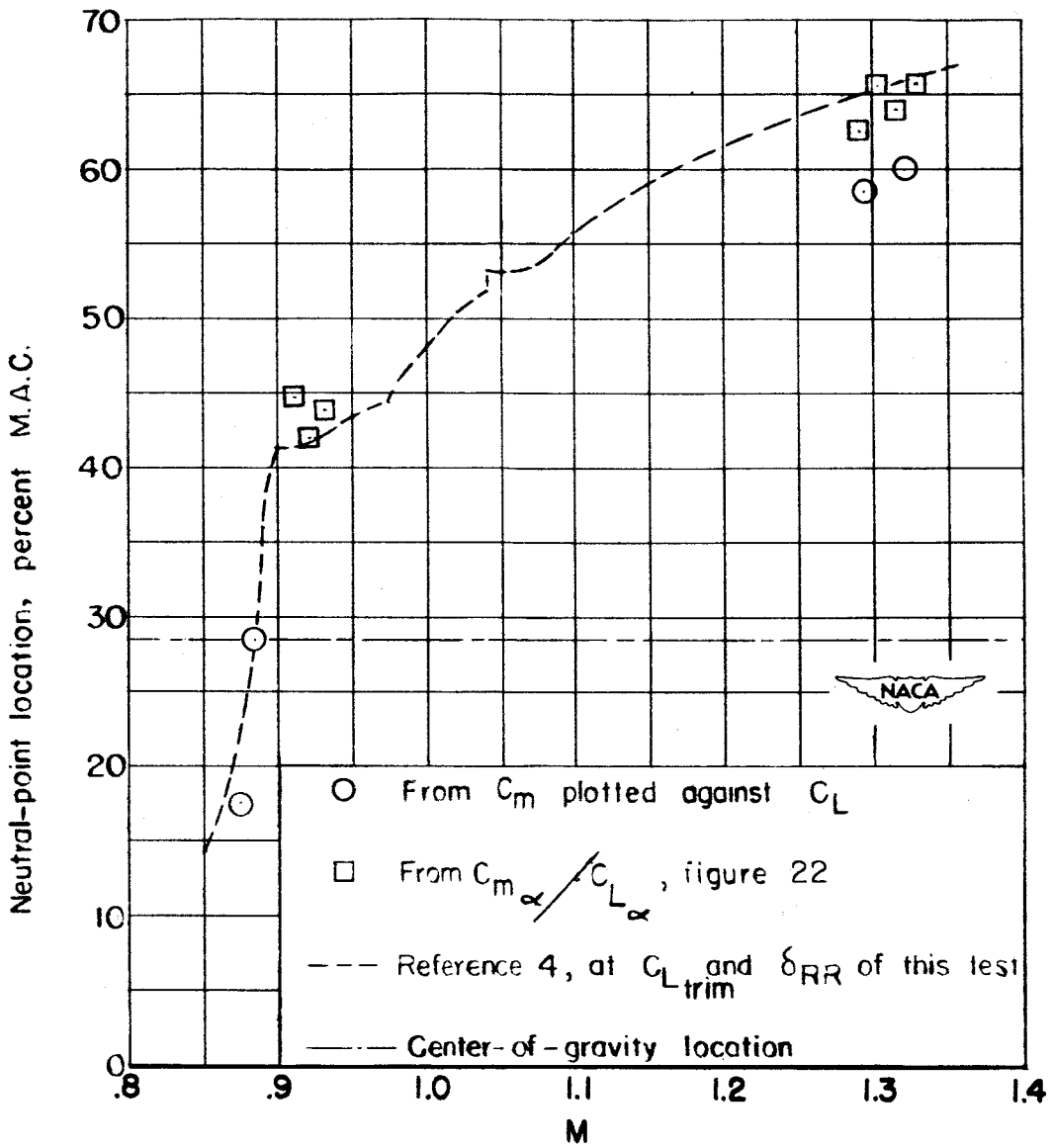

Figure 24.- Neutral-point location.

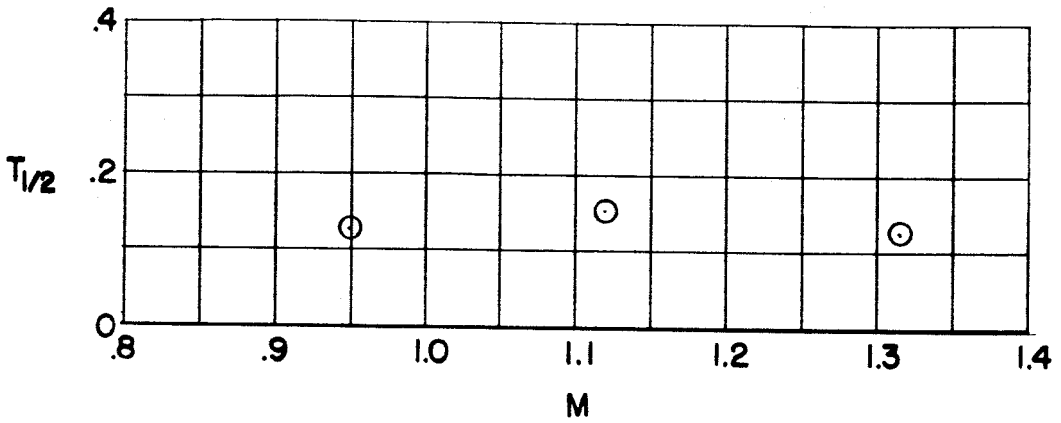

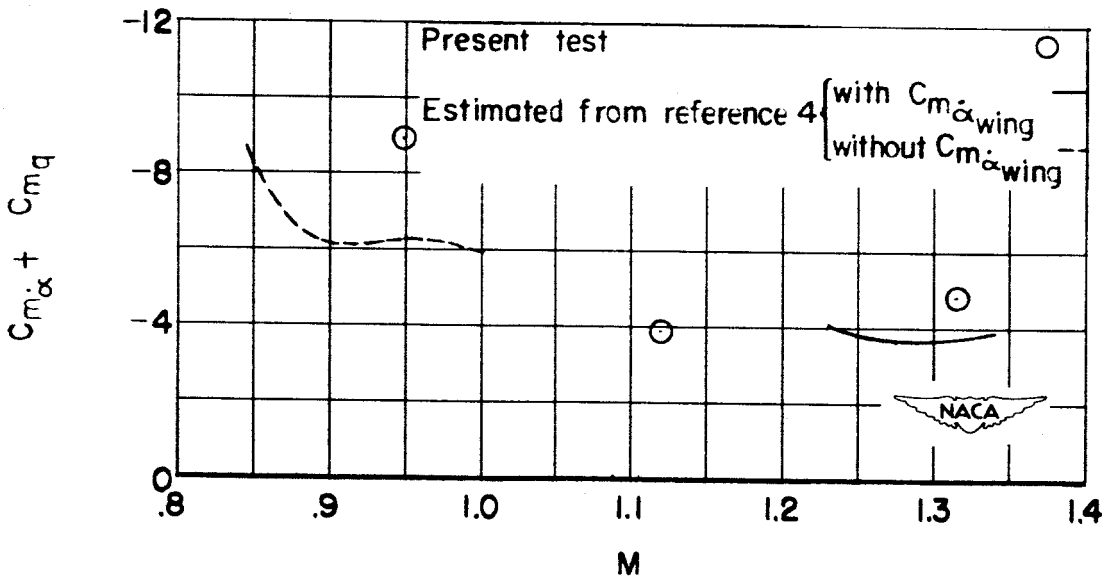

Figure 25.- Longitudinal dynamic stability parameters.

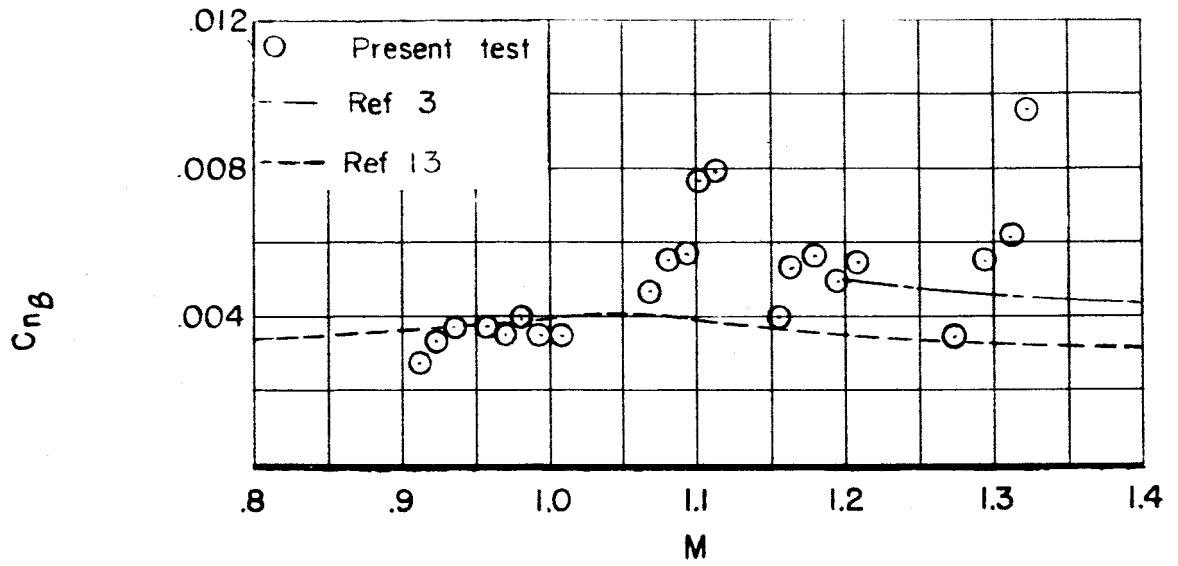

Figure 26.- Directional static stability derivative C_{n_β}.

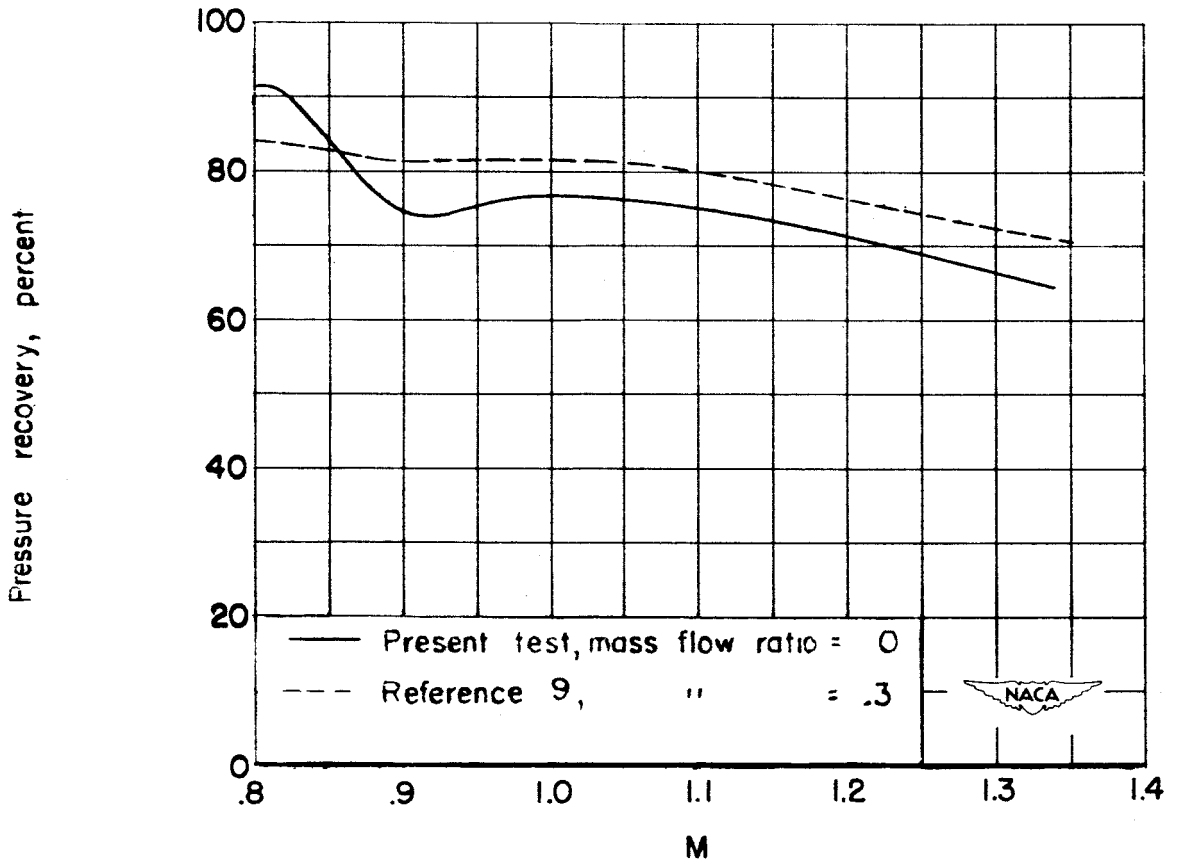

Figure 27.- Pressure recovery.